Available online at www.sciencedirect.com

ScienceDirect

Geochimica et Cosmochimica Acta 120 (2013) 395–416

Geochimica et Cosmochimica Acta

www.elsevier.com/locate/gca

# Natural age dispersion arising from the analysis of broken crystals: Part II. Practical application to apatite (U–Th)/He thermochronometry

Romain Beucher [a,1], Roderick W. Brown [a,*], Steven Roper [b], Fin Stuart [c], Cristina Persano [a]

[a] School of Geographical and Earth Sciences, College of Science and Engineering, University of Glasgow, Glasgow G12 8QQ, United Kingdom
[b] School of Mathematics and Statistics, College of Science and Engineering, University of Glasgow, Glasgow G12 8QQ, United Kingdom
[c] Scottish Universities Environmental Research Center, Rankine Avenue, Scottish Enterprise Technology Park, East Kilbride G75 0QF, United Kingdom

Received 5 November 2012; accepted in revised form 30 May 2013; available online 13 June 2013

**Abstract**

We describe a new numerical inversion approach to deriving thermal history information from a range of naturally dispersed single grain apatite (U–Th)/He ages. The approach explicitly exploits the information about the shape of the $^4$He diffusion profile within individual grains that is inherent in the pattern of dispersion that arises from the common and routine practice of analysing broken crystals. Additional dispersion arising from differences in grain size and in U and Th concentration of grains, and the resultant changes to helium diffusivity caused by differential accumulation and annealing of radiation damage, is explicitly included. In this approach we calculate the ingrowth and loss, due to both thermal diffusion and the effects of α-ejection, of helium over time using a finite cylinder geometry. Broken grains are treated explicitly as fragments of an initially larger crystal. The initial grain lengths, $L_0$, can be treated as unknown parameters to be estimated, although this is computationally demanding. A practical solution to the problem of solving for the unknown initial grain lengths is to simply apply a constant and sufficiently long $L_0$ value to each fragment. We found that a good value for $L_0$ was given by the maximum fragment length plus two times the maximum radius of a given set of fragments. Currently whole crystals and fragments with one termination are taken into account. A set of numerical experiments using synthetic fragment ages generated for increasingly complex thermal histories, and including realistic amounts of random noise (5–15%), are presented and show that useful thermal history information can be extracted from datasets showing very large dispersion. These include experiments where dispersion arises only from fragmentation of a single grain (length 400 μm and radius 75 μm, c. 6–50% dispersion), including the effects of grain size variation (for spherical equivalent grain radii between 74 and 122 μm, c. 10–70% dispersion) and the combined effects of fragmentation, grain size and radiation damage (for eU between 5 and 150 ppm, c. 10–107% dispersion). Additionally we show that if the spherical equivalent radius of a broken grain is used as a measure of the effective diffusion domain for thermal history inversions then this will likely lead to erroneous thermal histories being obtained in many cases. The viability of the new technique is demonstrated for a real data set of 25 single grain (U–Th)/He apatite ages obtained for a gabbro sample from the BK-1 (Bierkraal) borehole drilled through the Bushveld Complex in South Africa. The inversion produces a well constrained thermal history consistent with both the (U–Th)/He data and available fission track analysis data. The advantage of the new approach is that it can explicitly accommodate all the details of conventional schemes, such as the effects of temporally variable diffusivity, zonation of U and Th and arbitrary grain size variations, and it works equally effectively for whole or broken crystals, and for the most common situation where a mixture

* Corresponding author.
*E-mail addresses:* romain.beucher@geo.uib.no (R. Beucher), roderick.brown@glasgow.ac.uk (R.W. Brown).
[1] Principal corresponding author (now at University of Bergen, Department of Earth Science, P.O.Box 7803, N-5020 Bergen, Norway).

http://dx.doi.org/10.1016/j.gca.2013.05.042
0016-7037/

of both are analysed. For the routine application of the apatite (U–Th)/He thermochronometry technique with samples where whole apatite grains are rare our experiments indicate that 15–20 single grain analyses are typically required to characterise the age dispersion pattern of a sample. The experiments also suggest that picking very short crystal fragments as well as long fragments, or even deliberately breaking long crystals to maximise the age dispersion in some cases, would ensure the best constraints on the thermal history models. The inversion strategy described in this paper is likely also directly applicable to other thermochronometers, such as the apatite, rutile and titanite U–Pb systems, where the diffusion domain is approximated by the physical grain size.


## 1. INTRODUCTION

The (U–Th)/He thermochronometry technique is widely applied for quantifying the thermal histories of rocks at temperatures of c. 90–30 °C, which are characteristic of shallow crustal depths of c. 1–5 km (e.g., Farley, 2002; Ehlers and Farley, 2003; Reiners et al., 2005; Reiners and Brandon, 2006). Deriving the thermal history information from the measured grain ages for a rock sample requires the use of a model capable of calculating a predicted age as a function of the net ingrowth and diffusional loss of the daughter product within the effective diffusion domain for any given thermal history (e.g., Lovera et al., 2002; Meesters and Dunai, 2002b). Both laboratory and natural experiments have been used to constrain the kinetic parameters of thermal diffusion of helium in apatite (House et al., 1999; Farley, 2000, 2002; Cherniak et al., 2009; Shuster et al., 2006), and the results indicate that the rate of diffusion is isotropic and that the effective diffusion domain is the physical grain dimension. Additionally, it has been well demonstrated by several studies that the diffusion of helium within a hexagonal prism or finite cylinder can be accurately approximated by the modelling the diffusion of helium within a sphere which has the same volume to surface area ratio as the prismatic grain, i.e., the so called spherical equivalent radius, which we will call $R^*$ (Meesters and Dunai, 2002b; Gautheron et al., 2009; Watson et al., 2010). This approximation enables the calculations of diffusion to be performed in one-dimension (the spherical radial distance) and is therefore computationally much faster than using a two dimensional geometry required for finite prismatic or cylindrical geometries (e.g., Meesters and Dunai, 2002a,b; Watson et al., 2010). These experimental kinetic parameters and the spherical equivalent radius approximation underpin current approaches to deriving quantitative thermal history information from measured single grain (U–Th)/He (AHe) ages (e.g., Wolf et al., 1998; Ketcham, 2005; Gallagher, 2012).

It is implicit in all these approaches that the grains being analysed are whole crystals that have been extracted intact from the host rock. This is an important assumption for two reasons. Firstly, the spherical equivalent grain size calculated from the dimensions of the grain is only an accurate measure of the effective diffusion domain if it is determined using the true width and length of the whole crystal, and so if the grain is broken during mineral separation then the calculated SEQR will be too small (Fig. 1). Secondly, and most importantly, if the concentration of helium within the whole crystal is not uniform, which would be expected for all samples that have not experienced instantaneous cooling from high temperatures, then the ratio of $^4$He to parent U and Th in the crystal fragment is unlikely to be the same as in the whole grain and so the measured age will be either too old or too young (Brown et al., 2013, this volume). In such cases deriving a model thermal history from ages measured on broken grains from a sample, and using the $R^*$ approximation based on the broken grain dimensions, will likely lead to erroneous results.

Apatite grains extracted from rocks for AHe thermochronometry are often broken though because apatite has a weak basal cleavage and so the typically prismatic crystals routinely break into fragments along this cleavage plane, and this fact is well documented in the literature (e.g., Farley et al., 1996, 2010; Farley, 2002). Currently, in most laboratories, including University of Glasgow, it is common practice to multiply the length of a broken crystal by a factor of 1.5 unless the grains are demonstrably unbroken (Farley, 2002) for the purposes of calculating the $F_T$ correction factor (Farley et al., 1996) in recognition that the grains must have been larger and therefore will have lost less helium by$\alpha$-ejection than would appear if the actual fragment dimensions were used to calculate $R^*$. More sophisticated options for calculating the $F_T$ correction factor that considers the full geometry of grains as well as heterogeneous U and Th is possible (Ketcham et al., 2011; Gautheron et al., 2012). However, this practice only effects the calculation of the corrected age (i.e., age corrected for $\alpha$-ejection), and is never extended to modifying the raw grain ages and generally not used to calculate the effective spherical equivalent radii, $R^*$, of fragments for use in modelling the thermal histories of samples. We will discuss this specific problem in more detail below.

However, the major challenge to deriving thermal histories from AHe ages on single grains is the ambiguity that arises because different combinations of time and temperature can yield the identical age for any particular grain. So, without independent information to constrain the initial age of the rock, or the start of the history, it is always possible to find a spectrum of viable thermal histories that range between those that are short and cold and those that are long and hot. In each case the total amount of $^4$He that remains in the grain is identical because for the short-cold histories less $^4$He is accumulated but less is lost by diffusion because the temperatures are low, and vice versa for the long-hot histories. The key to discriminating between these different histories is that although the volume integral of the $^4$He concentration in the grain is identical for all histories the distribution of helium within the grain is not the same. The $^4$He/$^3$He technique (Shuster and Farley, 2005) was developed to exploit this fact, and uses an induced constant reference concentration of $^3$He, produced by proton

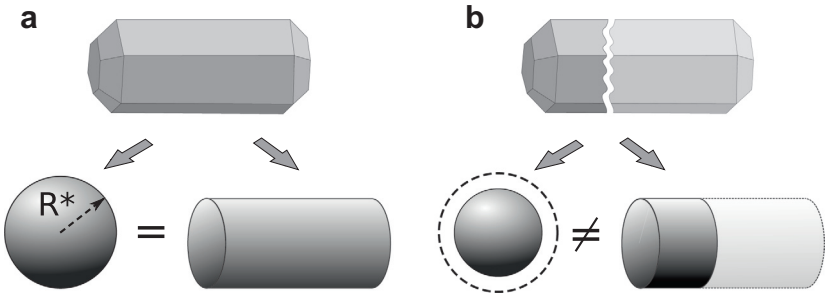


Fig. 1. Approximating hexagonal prismatic apatite crystals as finite cylinders and as spheres with an equivalent surface area/volume ratio. (a) Both approximations work well for whole, unbroken grains. (b) The spherical equivalent radius approximation is not appropriate for diffusion calculations when applied to broken grains because the true grain size and thus the effective diffusion domain size is underestimated.

irradiation of the grain, and a step-heating analytical approach to recover the shape of the natural $^4$He diffusion profile within the grain relative to the $^3$He reference (Shuster and Farley, 2004). This is an elegant solution to the problem but it is quite challenging analytically and it is expensive to apply routinely. An additional restriction is that it requires the analyses to be performed on intact, whole grains for the results to be reliable, particularly so for samples which have experienced a protracted thermal history and suffered a large degree (>c. 20%) of diffusional He loss (Farley et al., 2010).

For all samples that have not cooled rapidly through the helium partial retention zone (PRZ, c. 90–30 °C), but rather experienced protracted cooling through the PRZ or recent reheating to maximum palaeotemperatures of c. 60–90 °C, individual apatite grains extracted from the same sample should yield varying AHe ages for a variety of reasons. Useful, natural dispersion arises because of intrinsic differences in $^4$He retentivity of grains, such as differences in grain size (Reiners and Farley, 2001) and differences in U and Th abundance and the consequent effect on radiation damage accumulation (Shuster et al., 2006; Flowers et al., 2009; Gautheron et al., 2009). Other extraneous causes, such as the presence of U and Th rich micro-inclusions (Fitzgerald et al., 2006; Vermeesch et al., 2007), heterogeneous He injection from neighbouring grains (Spiegel et al., 2009; Gautheron et al., 2012), variable patterns of U and Th zonation (Farley et al., 2011; Ault and Flowers, 2012), produce dispersion that is unhelpful because it is unrelated to the thermal history of the sample. So called 'over-dispersion' of the AHe ages measured for single grains from the same sample is therefore a common observation (e.g., Fitzgerald et al., 2006; Kohn et al., 2009; Flowers and Kelley, 2011), and understanding what causes this dispersion is critical to interpreting measured ages properly (Flowers et al., 2007, 2008, 2009; Ault et al., 2009; Flowers and Kelley, 2011). In a companion paper (Brown et al., submitted for publication, this volume) we showed that a key component to understanding and utilising this dispersion behaviour arises from the fact that individual crystals that are analysed are often fragments of larger crystals. Importantly we demonstrated that dispersion caused by fragmentation is significant and contains useful information about the shape of the diffusion profile within grains and hence the thermal history of the sample, and that it also causes the expected relationships between AHe ages and grain size and eU to be corrupted.

Here we describe a new inversion approach to deriving thermal history information that simultaneously tackles the ambiguity problem and the fact that apatite grains are often broken. It utilises conventional AHe single grain analyses and so does not require proton irradiation of samples or the use of a sector mass spectrometer and exploits useful information recorded by the natural dispersion of AHe ages. The new approach explicitly exploits this fragment related component of the dispersion pattern using a set of synthetic examples. We also explicitly examine the effect of 'noise' potentially arising from micro-inclusions (Fitzgerald et al., 2006; Vermeesch et al., 2007), implantation of $^4$*He* by injection from neighbouring grains (Spiegel et al., 2009), or heterogeneous [U] and [Th] concentration. The practical viability of the new method is then demonstrated using a real data set.

## 2. MODELLING SINGLE AGES

To model the evolution of the AHe age of a grain over time requires calculating the net accumulation of $^4$He within the grain which is a function of the natural ingrowth of $^4$He from the radioactive decay of U, Th and Sm balanced by the loss of $^4$He by α-ejection and any thermally activated diffusion of helium out of the grain. Most of the diffusion models used to model AHe ages use the SEQR approximation because it is computationally efficient (e.g., Meesters and Dunai, 2002b; Ketcham, 2005; Gautheron and Tassan-Got, 2010; Gallagher, 2012), which is an important consideration for inversion schemes where typically many thousand forward thermal history models are evaluated. However, this approach implicitly collapses the axial and radial components of diffusion within prismatic crystals onto asingle radial dimension. This simplification is valid if the analysed grain was intact (Fig. 1a), but not if the grain was broken during extraction from the host rock (Fig. 1b). This is because the combination of axial and radial diffusion in an elongated, prismatic crystal causes the tips of the grain to be much more depleted in $^4$He than the outer surface of the central prismatic part of the crystal. Apatite grain fragments typically break along the cleavage perpendicular to the prismatic *c*-axis, and so apatite grain fragments can be thought of conceptually as slices of

varying size cut perpendicular to the *c*-axis from an originally longer crystal.

To quantitatively consider the effects of this type of fragmentation of apatite grains on measured AHe ages we have developed a practical model based on a simple finite cylinder geometry. In this section, we detail an analytical solution for thermally activated diffusion within the finite cylinder with a uniform source, including the effects of ejection of $^4$He due to the long α-stopping distances in apatite (Farley et al., 1996; Ketcham et al., 2011). We assume that the helium concentration boundary set on the outer surface of the crystals is zero. The purpose of the model is to provide a practical basis for modelling AHe ages of whole grains as well as fragments which will underpin the new inversion approach, and we employ a similar mathematical approach to that taken by Meesters and Dunai (2002a,b) andWatson et al. (2010). The analytical solution accounts for anisotropic diffusion (although not used here for apatite) and can be easily adapted to include the effects of a heterogeneous initial distribution of $^4$He or of the source (i.e., [U], [Th], [Sm] concentrations).

### 2.1. Geometry and diffusion equation: the finite cylinder approximation

A list of all model parameters and variables is provided with explanations in Table A1. A finite cylinder occupies the region $0 \leqslant z \leqslant L_0$ and $0 \leqslant r \leqslant R_0$ where $z$ and $r$ are the axial and radial dimensions, respectively (Fig. 2a). Helium diffuses isotropically in apatite (e.g., Cherniak et al., 2009) according to the diffusion equation (e.g., Watson et al., 2010), and using cylindrical coordinates this can be written as

$$\frac{\partial C}{\partial t} = D\frac{\partial^2 C}{\partial z^2} + D\frac{1}{r}\frac{\partial}{\partial r}\left(r\frac{\partial C}{\partial r}\right) \tag{1}$$

with $D$ being the diffusivity which depends on temperature $T(t)$, which may depend on the time $t$, and which follows an Arrhenius law of the form

$$D = D_0 \exp\left[-\frac{E_a}{RT(t)}\right] \tag{2}$$

where $D_0$ is the diffusivity at infinite temperature and $T(t)$ is the dimensional temperature at time $t$. The activation energy $E_a$ is a constant and $R$ is the molar gas constant.

$^4$He is produced by the decay of the radioactive parent isotopes $^{238}$U, $^{235}$U, $^{232}$Th and $^{147}$Sm. Let the number of different parent isotopes that contribute to the production of helium be $N$, and the concentration of parent isotope $i$ be $P_i(r,z,t)$. The isotopes are immobile and decay with decay rate $\alpha_i$. The ingrowth of helium is therefore produced by α-decay of the parent isotopes and each parent isotope $i$ produces $n_i$ helium nuclei. The equation for the reduction in concentration of parentisotope $i$ because of radioactive decay is then

$$\frac{\partial P_i}{\partial t} = -\alpha_i P_i \tag{3}$$

which has the solution

$$P_i(r,z,t) = P_i^f(r,z)e^{\alpha_i(t_f - t)} \tag{4}$$

so production of helium by each parent isotope $i$ is

$$C_i(r,z,t) = n_i P_i^f(r,z)e^{\alpha_i(t_f - t)} \tag{5}$$

and the concentration of each parent isotope at the end of the model time is $P_i(r,z,t_f) = P_i^f(r,z)$, with $t$ being the time and $t_f$ being the total model time (model time starts at $t = 0$).

### 2.2. The α-ejection effect

Helium nuclei are ejected from their parent nucleous with a range of energies and in random directions. If the parent nucleous of a helium atom is located near the surface of the grain then the long stopping distances for α-particles in apatite (c. 20 μm) cause some of helium nuclei to be lost immediately by ejection out of the grain (Farley et al., 1996; Ketcham et al., 2011). One way to account for α-particle ejection is to alter the production of helium from the source

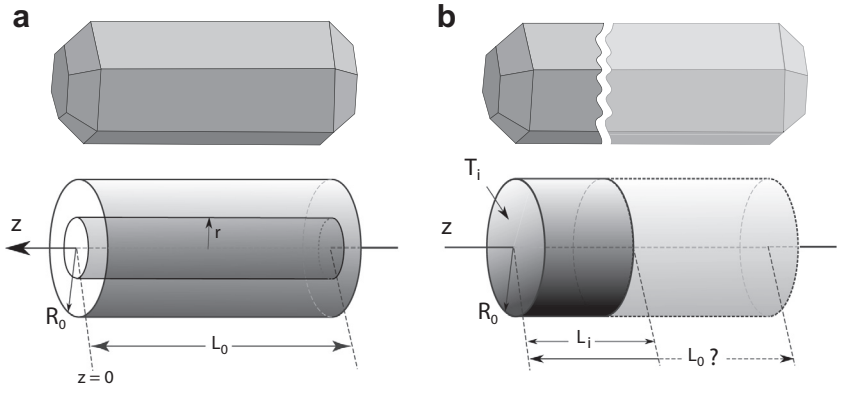


Fig. 2. Model geometry and parameterisation. (a) Whole grains are approximated using a finite cylinder geometry with specified whole grain length, $L_0$, with cylindrical radius, $R_0$. (b) Broken grains are specified as parts of a whole grain using the actual fragment length, $L_i$, and the observed grain cylindrical radius, $R_0$ (half width). Fragments with 1 termination (1T fragments) begin at one end of the cylinder for the model whole grain and extend for distance $L_i$ along the axial direction. Fragments with no terminations (0T fragments) are specified similarly but are centred within the whole grain cylinder accordingly.

in an appropriate manner within a region near the surface of the grain. So, rather than generating helium uniformly and then ejecting some of it, the source distribution can be modified so that the helium that would have been ejected is simply not generated during each model time step. This means that the effective source term for helium is not uniform (even for a uniformdistribution of parent isotopes $P_i(r,z,t)$).

To account for α-particle ejection we can modify the source term for each parent isotope (see Eq. (5)) by multiplying the source term by some linear operators $\mathcal{L}_i$ that depend on the details of decay for each isotope. The $\mathcal{L}_i$ operator we use here (details are provided in Appendix A) has the property such that it is 1/4 near the corners, 1/2 near the edges and 1 in the interior, varying smoothly between these values over the stopping distance $S_i$. Note that this function can be easily modified to account for alternative α-ejection models and to account for heterogeneous spatial distributions of the parent isotopes, but this is beyond the scope of this paper.

Combining the modified source terms defining the ingrowth of helium (Eq. (5)) with the term describing the thermal diffusional loss of helium (Eq. (1)) yields the combined production–diffusion equation for calculating the concentration of helium as a function of time

$$\frac{\partial C}{\partial t} = D\frac{\partial^2 C}{\partial z^2} + D\frac{1}{r}\frac{\partial}{\partial r}\left(r\frac{\partial C}{\partial r}\right) + \sum_{i=1}^{N}\alpha_i n_i \mathcal{L}_i\left[P_i^f(r,z)\right]e^{\alpha_i(t_f-t)} \quad (6)$$

### 2.3. Allowing for an arbitrary thermal history

The thermal history can be represented by an arbitrary number of temperature–time pairs with the temperature varying linearly between segments. A neater, generic non-dimensional solution follows if we introduce some simple scaling parameters. If we assume that the thermal history occurs on a time scale $\tau_e$, then the non-dimensional model time is written as $t' = t/\tau_e$ and the final model time is $t'_f = t_f/\tau_e$ (i.e., the total duration of the thermal history). The time can be scaled by any convenient value, and here we use a value of 1 Ma for $\tau_e$, which is appropriate for geological timescales. The dimensional cylindrical radius of the crystal is $R_0$ and its length is $L_0$, so the non-dimensional length scales are obtained by dividing by $R_0$, so that the non-dimensional radius $r$ is equal to 1 and the non-dimensional length is $l = L_0/R_0$.

If we define a suitable temperature scale by an appropriate range $\Delta T = T_{\max} - T_{\min}$ the temperature can be written in terms of the range $\Delta T$ and the maximum temperature $T_{\max}$ such that $T(t) = T_{\max} - \Delta T\theta$ with $\theta$ between 0 and 1. This allows us to write Eq. (2) in terms of the temperature range, $\Delta T$, and $\theta$, such that

$$D = D_0 \exp\left[-\frac{E_a}{RT_{\max}}\right]\exp\left[-\frac{\Delta T E_a}{RT_{\max}^2}\frac{\theta}{1-\delta\theta}\right] \quad (7)$$

$$= \hat{d}\exp\left[-\frac{\gamma\theta}{1-\delta\theta}\right] \quad (8)$$

where

$$\hat{d} = D_0\exp\left[-\frac{E_a}{RT_{\max}}\right], \qquad \gamma = \frac{E_a\Delta T}{RT_{\max}^2}, \qquad \delta = \frac{\Delta T}{T_{\max}}. \quad (9)$$

The characteristic timescale of diffusion at the maximum temperature, $T_{\max}$, is given by

$$\tau_d = R_0^2/\hat{d} \quad (10)$$

and combining this characteristic diffusion timescale with the characteristic time scale for the model thermal history, $\tau_e$, we can define the temporal scaling parameter $\beta = \tau_e/\tau_d$.

Now let a characteristic scale for the concentration of both helium and the parent isotopes be $\bar{C}$, and scale the concentration of helium such that the non-dimensional helium concentration is $c = C/\bar{C}$ and similarly for the parent isotopes such that $p_i = P_i/\bar{C}$. The decay rates, $\alpha_i$, for the parent isotopes are also scaled by $\tau_e$ to give the values $\lambda_i = \alpha_i\tau_e$.

So, including all the scaling factors defined above into Eq. (6) gives the equation for the non-dimensional helium concentration as

$$\frac{\partial c}{\partial t'} = \beta\left(\frac{1}{r}\frac{\partial}{\partial r}\left(r\frac{\partial c}{\partial r}\right) + \frac{\partial^2 c}{\partial z^2}\right)\exp\left[-\frac{\gamma\theta}{1-\delta\theta}\right] + \sum_{i=1}^{N}\mathcal{L}_i\left[p_i^f\right]\lambda_i n_i e^{\lambda_i\left(t'_f - t'\right)} \quad (11)$$

Eq. (11) is solved on the non-dimensional domain $0 \leqslant r \leqslant 1$ and $0 \leqslant z \leqslant l$, with boundary conditions $c = 0$ on the boundary of the cylinder. The solution is written in terms of eigenmodes which are obtained by multiplying Eq. (11) by $rJ_0(\alpha_m r)\sin(n\pi z/l)$ where $\alpha_m$ is the $m$th zero of the Bessel function $J_0(r)$ and integrating over the volume of the cylinder.

Then, with the orthogonality of the eigenmodes, this leads to a series of $(m \times n)$ mode equations

$$\frac{\partial c_{nm}}{\partial t'} = -\beta\left(\alpha_m^2 + \frac{n^2\pi^2}{l^2}\right)c_{nm}\exp\left[-\frac{\gamma\theta}{1-\delta\theta}\right] + \sum_{i=1}^{N}\lambda_i n_i e^{-\lambda_i\left(t'_f - t'\right)} \frac{4}{lJ_1(\alpha_m)^2}\int_{z=0}^{l}\int_{r=0}^{1}\mathcal{L}\left[p_i^f\right]\sin\left(\frac{n\pi z}{l}\right)J_0(\alpha_m r)\,r\,dr\,dz \quad (12)$$

where the appropriate initial conditions are given as

$$c_{nm}(0) = \frac{1}{l}\int_0^l dz\int_0^1 dr\; rJ_0(\alpha_m r)\sin\left(\frac{n\pi z}{l}\right)c_{\text{init}}(r,z)\;dr \quad (13)$$

The integrals in Eq. (12) are required to account for loss of helium by α-ejection and are encoded in the linear operators $\mathcal{L}_i$ (see Appendix A.5 for details). Including the appropriate integrals into the mode equations defined in Eq. (12) gives the final set of $m \times n$ mode equations which can now be written as

$$\frac{\partial c_{nm}}{\partial t'} = -\beta\left(\alpha_m^2 + \frac{n^2\pi^2}{l^2}\right)c_{nm}\exp\left[-\frac{\gamma\theta}{1-\delta\theta}\right] + \sum_{i=1}^{N}\lambda_i n_i e^{\lambda_i\left(t'_f - t'\right)}p_i^f M_{nm} \quad (14)$$

The mode equations (14) can now be solved for each segment of any arbitrary, piecewise linear, thermal history specified by an array of time-temperature points $\left(t'_j, \theta_j\right)$ for $j = 1$ to $k$, where $k$ is the number of time–temperature points. The equations are solved successively for each segment of the thermal history, where the initial condition for each segment is just the solution obtained for the preceding segment. We assume that the initial condition $c_{nm}(0)$ at the start of the history at time $t'_0 = 0$ is zero.

The final solution for the non-dimensional helium concentration $c(r,z,t')$ is then obtained by summing over all of the $m \times n$ eigenmodes

$$c(r,z,t') = \sum_{n,m} c_{nm}(t') r J_0(\alpha_m r) \sin\left(\frac{n\pi z}{l}\right). \tag{15}$$

where $c_{nm}(t')$ indicates the solution for each of the eigenmodes defined by Eq. (14). The total amount of helium (non-dimensional) contained in a section of the cylinder from $z = z_1$ to $z = z_2$ at time $t'$ is

$$\mathcal{C}^n(t', z_1, z_2) = 2\sum_{n,m} c_{nm}(t') \times \frac{1}{\alpha_m n} J_1(\alpha_m) l\left(\cos\left(\frac{n\pi z_1}{l}\right) - \cos\left(\frac{n\pi z_2}{l}\right)\right) \tag{16}$$

and the total dimensional amount of helium (in moles, $\mathcal{M}^d$) is

$$\mathcal{M}^d(t', z_1, z_2) = \overline{C} R_0^3 \mathcal{C}^n(t', z_1, z_2) \tag{17}$$

and the dimensional concentration of helium within the slice, $\mathcal{C}^d$, is the total amount within the slice divided by the volume of the slice

$$\mathcal{C}^d = \frac{\mathcal{M}^d}{\pi R_0^3 |z_2 - z_1|} = \frac{\overline{C}\mathcal{C}^n}{\pi |z_2 - z_1|} \tag{18}$$

### 2.4. Dealing with fragments

A key parameter in the (U–Th)/He technique is the effective size of the diffusion domain which in the case of apatite is the physical grain size. The dimensions of analysed grains are therefore routinely measured with the grain length and width/s being accurately recorded. It is also good practice to record whether the grains are broken or not, and if they are to also record how many terminations each grain has, i.e., either a whole crystal with 2 terminations (2T grain), 1 termination (one end intact the other broken, 1T grain) or none (both ends missing, 0T grain). These dimensions are needed for the calculation of the grain volume (to enable He, U, Th and Sm concentrations to be determined), making any correction to the measured age that attempts to account for the α-ejection effect and for input into thermal history models. As discussed above, it is usual to determine a spherical equivalent radius of some kind (Meesters and Dunai, 2002b; Ketcham et al., 2011) for the purposes of modelling the observed ages implicitly assuming that all the grains are whole crystals with both terminations intact. In this model we explicitly treat grains with 1 or no terminations as fragments of an initially larger grain, or as whole grains with both terminations intact, as appropriate (Fig. 2b). So for modelling purposes we explicitly specify the grain cylindrical radius $R_0$ (half width) and the initial whole grain length $L_0$ and determine the $^4He$ concentration within the whole grain. For 2T grains (whole grains) the integration of the model $^4He$ concentration is simply performed over the whole cylinder from $z = 0$ to $z = L_0$. For 1T fragments we effectively cut the appropriate fragment length, $L_i$, from this cylinder using the observed fragment length and perform the integration of the $^4He$ concentration from $z = 0$ to $z = L_i$. For fragments with no terminations the same approach is used and the integration is simply performed between the two appropriate $z$ co-ordinates.

### 2.5. Implementation

For each grain the array of ordinary differential equations (ODE) specifying all of the eigenmode equations obtained from Eq. (14) were solved using the LSODA solver from the ODEPACK collection of ODE solvers (Hindmarsh, 1983). The length of the time step through the arbitrary $t$–$T$ path (specified as a set of linear $t$–$T$ segments) is automatically chosen by the ODEPACK solver as a function of the complexity of the problem being solved. The $t$–$T$ history is passed to the solver as an array of $t$–$T$ points together with the mode equation to be solved. The effect of helium loss caused by α-ejection is explicitly accounted for at each time step as described inSection 2.2 and so the predicted model AHe ages are equivalent to the raw, uncorrected ages as would be measured in the laboratory. Compilable source code demonstrating this implementation is provided in the Electronic Annex.

Following Gautheron et al. (2012) we routinely also calculate the concentration of $^4$He in every grain assuming no α-ejection takes place, and the 'ejection free' AHe ages calculated using these concentrations could be thought of as being equivalent to the $F_T$ corrected ages following the practice of Farley et al. (1996) and more recently Ketcham et al. (2011). However, for the purposes of this paper we are interested in extracting the thermal history information of a sample and so we are only concerned with modelling the raw, uncorrected AHe ages. For comparison purposes the ages for all cylindrical grains are also routinely calculated using the SEQR approximation and a 1D spherical solution (seeAppendix B).

As pointed out by Meesters and Dunai (2002b) solving the eigenmode equations for a spherical geometry typically requires summation over only 15 or so eigenmodes. In the case of a finite cylindrical geometry, the number of eigenmodes to consider is at least $15^2$. In our code (HelFrag) the number of eigenmodes used in the radial direction is entered as an input parameter and the number of eigenmodes used in the axial direction is then scaled according to the aspect ratio of the grain under consideration. We chose a conservative approach and typically specified 30 eigenmodes in the radial direction. At the end of the $t$–$T$ path, all the eigenmode values are summed and converted to concentrations as shown in Eqs. (17) and (18).

## 3. EVALUATING THE MODEL AND THE ADVANTAGE OF USING A FINITE CYLINDER GEOMETRY

To evaluate and quantify the effects of fragmentation in the context of deriving thermal history information from a set of single grain AHe ages from a sample we performed a set of systematic numerical experiments (summarised in Table EA-1) for a range of thermal histories (Fig. 3a). The five histories we have selected are those used initially by Wolf et al. (1998) and we will refer to the $T$–$t$ paths as WOLF-1, 2, 3, 4 and 5 respectively. All five histories start at 100 Myr before present. WOLF-1 corresponds to a rapid cooling from temperatures above the Partial Retention Zone (PRZ) at 40 Ma and illustrates the evolution of a rapid, monotonic cooling history as might apply to a volcanic rock. All of the other histories include significant periods within the PRZ. WOLF-2 corresponds to a slower monotonic cooling from 135 °C that could be experienced during long-term erosional exhumation. In WOLF-3 the samples are held to at an isothermal temperature of 60 °C within the PRZ for 80 Myr and then cool linearly for the last 20 Myr as might occur subsequent to a tectonic event. WOLF-4 is very similar to WOLF-3 but starts with a 25 Myr period of linear cooling from 100 °C to 60 °C and has a less abrupt cooling to the surface. WOLF-5 illustrates a thermal history that might represent constant burial within a subsiding sedimentary basin. Here the sample is heated slowly up to 64 °C from a surface temperature of 15 °C over a period of 95 Myr and then cools linearly back to the surface temperature starting at 5 Myr. Although each history is quite different, they all produce AHe ages of c.

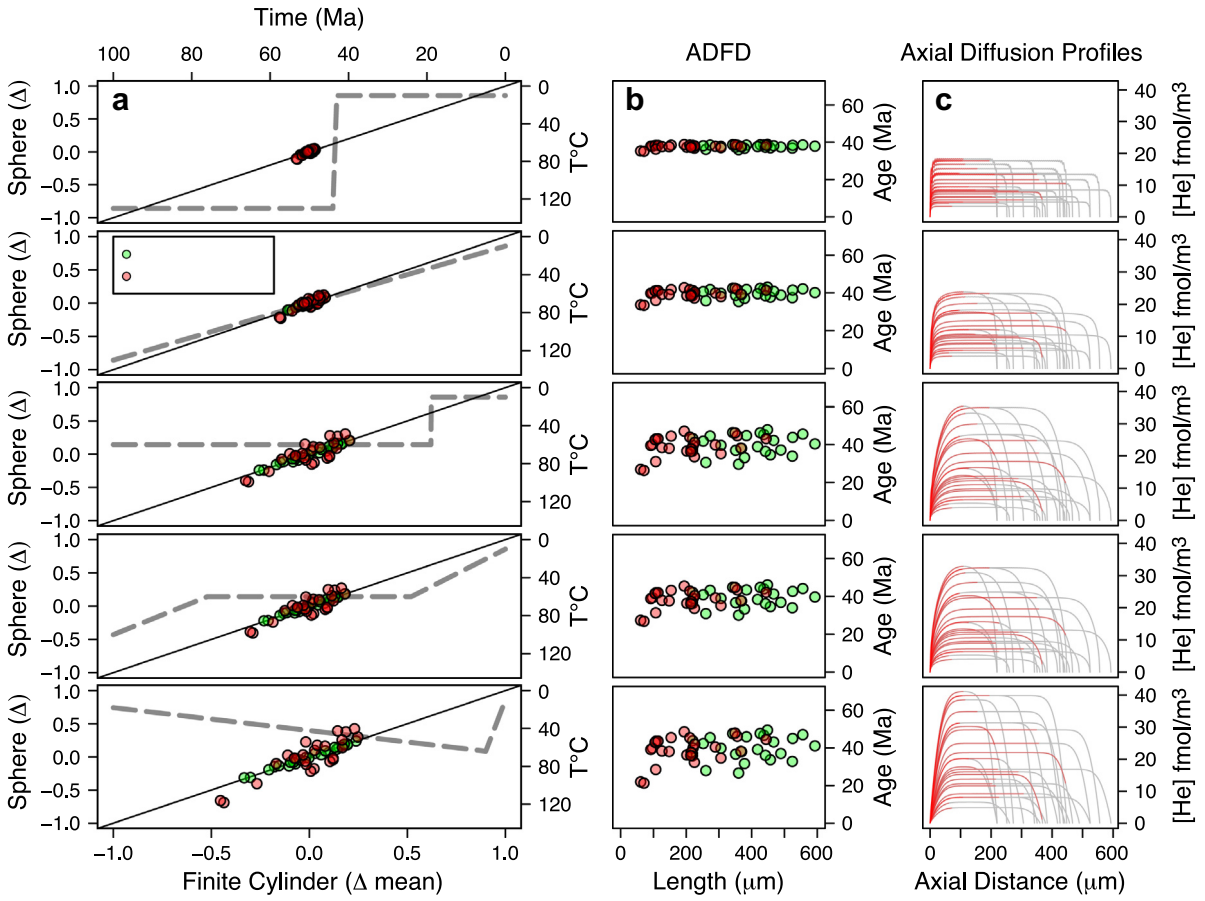


Fig. 3. Comparing spheres with finite cylinders. Model AHe ages were determined for each of the five thermal histories (WOLF-1 to 5) for a random set of 25 whole cylindrical grains, and 25 random fragments cut from these grains using the finite-cylinder geometry model. The AHe ages for all the grains and fragments were then also calculated using a spherical geometry (see Appendix B) and using the spherical equivalent radius approximation. The red circles indicate the ages for the fragments and the green circles those for whole grains. (a) Plot comparing the single grain AHe ages (deviation from the mean) calculated using both the spherical and cylindrical models. Grey dashed lines indicate the $t$–$T$ history for each model. Note that the ages for whole grains (green circles) always plot along the 1:1 line, irrespective of the amount of age dispersion, indicating that the two model geometries are equivalent for whole grains. The fragment ages (red circles) scatter around the 1:1 line though when there is significant age dispersion indicating that treating fragments as though they were spherical whole grains is inappropriate. (b) Age dispersion fragment distribution (ADFD) plots, showing the AHe ages determined using the finite-cylinder model geometry plotted versus fragment length. Note there is little age dispersion for the WOLF-1 history, but increasing amounts for the other histories, with most dispersion occurring for the fragment ages. (c) Plot showing all the axial helium diffusion profiles for the whole grains (grey lines) and for the fragments (red lines). Note that the profiles are flat for WOLF-1 and become increasingly "rounded" for the other histories. See text for detailed discussion. (For interpretation of the references to colour in this figure legend, the reader is referred to the web version of this article.)

40 Ma for a standard spherical equivalent grain size of 75 μm at a final surface temperature of 15 °C. Although the five histories yield similar standard AHe ages it is clear that each history produces very different $^4$He diffusion profiles within each of the grains (Fig. 3c).

### 3.1. Spheres versus cylinders, Model#1

The first experiment was designed to demonstrate the effect that fragmentation has on the pattern and amount of dispersion as a function of the thermal history, and specifically to evaluate the error that arises when fragments of larger grains are improperly treated as whole grains and their size is represented using the SEQR approximation (Fig. 2). We calculated the AHe ages for 24 random 2T whole grains (SEQR between 74 and 122 μm, initial [U] and [Th] both 20 ppm) and 24 1T fragments cut randomly from these grains for each of the WOLF thermal histories. In all experiments we use the diffusion parameters of Farley (2000) for $^4$He in apatite (i.e., $D_0 = 0.00316\ \mathrm{m^2\ s^{-1}}$ and $E_a = 138\ \mathrm{kJ\ mol^{-1}}$). The AHe ages for both whole grains and fragments were calculated using our finite cylinder model geometry and also using a simple 1D spherical solution to the ingrowth-diffusion equation (see Appendix B) and the standard SEQR approximation. The SEQR radii of fragments, $R_f^*$, were calculated using the fragment dimensions, and SEQR radii for whole grains, $R_g^*$, were calculated in the normal way using the true whole grain dimensions according to

$$R_g^* = \frac{3R_0L_0}{2(R_0 + L_0)} \tag{19}$$

and

$$R_f^* = \frac{3R_0L_i}{2(R_0 + L_i)} \tag{20}$$

The results of these experiments are summarised in Figs. 3, EA-2 and EA-3, and detailed fragment lists are provided in the Electronic Annex. The AHe ages obtained for each of the five WOLF histories using the finite cylinder model geometry are compared with the ages obtained using the spherical model geometry in Fig. 3a and b. Two important observations can be made from this comparison. Firstly, the amount of dispersion clearly varies between each of the five histories, with very little dispersion shown for WOLF-1, and progressively increased dispersion for the histories causing increased helium loss and consequently more rounded $^4$He diffusion profiles in the grains (Fig. 3c). This phenomenon is described in detail in a companion paper (Brown et al., 2013, this volume). Importantly, the ages for the whole grains (or deviations from the mean in this case) consistently plot along the 1:1 lines in Fig. 3a irrespective of the amount of dispersion. This empahsises that the SEQR approximation works well when applied to whole grains. In contrast, the ages for the 1T fragments diverge significantly from the 1:1 line, with the divergence increasing with increasing dispersion. This clearly illustrates the problem of treating fragments of larger crystals as whole grains and using the SEQR approximation and a spherical model to model the ages of these fragments. The ages determined on fragments are clearly not equivalent when modelled using the two different geometries, with the amount of divergence increasing with the degree of diffusional helium loss. The problem arises for two reasons. The first is that the $R_f^*$ values for fragments calculated using the fragment dimensions underestimates the effective diffusion domain size, and the second is because if the distribution of $^4$He within the whole grains is not homogeneous then this heterogeneity is not captured by a spherical solution which treats the fragments as whole, radially symmetric grains. This experiment clearly illustrates the advantage of explicitly treating broken grains as fragments of larger crystals using a finite cylinder, or other, appropriate approximation.

The amount of dispersion illustrated for these five histories clearly highlights the ambiguity issue that arises if a single, discrete AHe age is used to represent a sample. The pattern of age dispersion closely correlates with the thermal history and is effectively shown by plotting the ages on age dispersion fragment distribution (ADFD) plots (Fig. 3b) which plots fragment age versus fragment length. It is clear that the general shape of age the versus fragment length trajectories on these ADFD diagrams mimics the degree of 'roundness' of the axial diffusion profiles of $^4$He concentration in the grains (Fig. 3c). These patterns and how they relate to the thermal history and other grain attributes is described in detail in a companion paper (Brown et al., 2013, this volume).

The purpose of the numerical experiments described below are to demonstrate firstly how the natural dispersion arising from fragmentation alone can be practically used to resolve between these five thermal histories using a new inverse approach, and then to extend this approach to include dispersion arising from grain size and radiation damage effects.

## 4. INVERSE MODELLING APPROACH AND RESULTS FOR EXPERIMENTS USING SYNTHETIC DATA

Our intention in this paper is to describe the essential details of a new way of formulating the forward problem that forms the basis of the inverse approach to deriving thermal histories. In the following sections we make use of the Neighbourhood Algorithm (NA) (Sambridge, 1999a,b) which is an efficient and widely used algorithm designed for optimising the parameter search for multidimensional models (e.g., Herman et al., 2010, ; Valla et al., 2010, 2012; Glotzbach et al., 2011; Beucher et al., 2012). Improvements to the efficiency and design of the inversion procedure, particularly in the way in which the $t$–$T$ history is parameterised and the model misfit is evaluated, are certainly possible, but we emphasise this aspect of the approach is not the focus of the current paper.

### 4.1. Optimisation method

Our inversion method simply combines the finite cylinder based forward model described above with the NA scheme for parameter exploration. The NA code performs

a direct search for the model parameters in a multidimensional parameter space in order to optimise an evaluation function. We use the mean squared deviation, $\sigma^2$, between the observed and predicted AHe ages calculated for all grains in the model as the evaluation function to be minimised. This is calculated as the mean squared deviation of predictions of the AHe ages, $P_i$, compared with observations, $O_i$, for a set of $N$ crystals (here these are the synthetic AHe ages initially calculated for each of the WOLF histories using the forward model).

$$\sigma^2 = \frac{\sum_{i=1}^{N}(O_i - P_i)^2}{N} \quad (21)$$

The time–temperature history for each model is specified as a set of $t$–$T$ pairs and we assume linear heating or cooling segments between these pairs. In all the experiments described here we specified four $t$–$T$ pairs, although it is clear in some cases some pairs are redundant (e.g., WOLF-2). So, given a set of AHe ages for a number of grains of known length and radius, with known kinetic parameters $D_o$ and $E_a$ (we assume these are known and fixed for these experiments). The unknown model parameters that we need to fit are therefore the four $t$–$T$ pairs defining the thermal history. For each of the fragments we have an additional unknown parameter, the initial length of the grain, $L_0$. These parameters can be treated as unknowns and estimated directly as part of the inversion (see Fig. EA-1 Supplementary material), but we demonstrate below that this is unnecessary in practice and that the unknown initial lengths can be approximated by a choosing a suitably large and constant value for $L_0$.

A high-performance computing cluster (ScotGrid) was used to run 20,000 forward models for each inversion in order to provide accurate estimates of parameter values, given the number of free parameters in these inversions. Convergence of the algorithm is assessed by looking at the evolution of misfit through time; convergence is expected when the misfit becomes stationary. As described by Sambridge (1999a), the final model ensemble can be re-sampled to provide Bayesian measures of marginal probability-density functions (PDFs) for all fitted parameters, allowing quantitative assessment of the precision with which these parameters are resolved.

### 4.2. The problem of the initial length ($L_0$)

It follows from the discussion so far that calculating a model AHe age for any grain requires knowing the true grain dimensions, and so for fragments this means we need to know the actual initial length, $L_0$, of the unbroken crystal. This is clearly an unknown parameter for real grains extracted from a rock. However, we demonstrate that the problem can be significantly simplified for practical purposes for 1T fragments by substituting a constant value for $L_0$ which is sufficiently large. This simplification arises from the observation that the effects of axial diffusion extend inwards into the grains only to a maximum distance approximated by $R_0$, the cylindrical radius. This means that within the 'core' section of a prismatic grain, i.e., an interior section of the grain further than $R_0$ from both of it's tips, diffusion of helium is insensitive to the length of the crystal and determined only by $R_0$ and the thermal history.

Taking the example of a fragment with one termination (1T) and looking at the axial diffusion profiles we show that two distinct cases exist, which we refer to as Type I (Fig. 4a) and Type II (Fig. 4b), respectively. In the first case (Fig. 4a), the fragment comes from a significantly longer grain and contains only one tip effected by axial diffusion, so the fragment length $L_i$ is less than $L_0 - R_0$ (Type I). In the second case (Fig. 4b), the fragment length is close to $L_0$ and contains part of the second extremity effected by axial diffusion and so $L_i$ is greater than $L_0 - R_0$ (Type II).

In Fig. 4a and b we plot the calculated model AHe ages determined for a range of fragments of different aspect ratio (constant $R_0$) against a range of estimates of the initial grain length, $L_0$. For both the Type I and Type II fragments it is clear that if $L_0$ is chosen to be less than the true initial grain length then the model AHe age is too young. This effect is significant for all grains, and reaches a maximum for grains with lowest aspect ratios (the tips are proportionally more important for these grains). Obviously, if the correct $L_0$ is chosen then the model AHe age is correct for both Type I and Type II grains. However, it is significant and useful that for Type I grains choosing an $L_0$ value that is too long has no effect on the model AHe age determined for the fragment (Fig. 4a). In the case of a Type II fragments the apparent model AHe age increases slightly for $L_0$ values that are too long, but interestingly quickly approaches a constant plateau age (Fig. 4b). In detail, this effect for Type II fragments depends on the degree of degassing and therefore on the original grain geometry and the thermal history. Our experiments show that for extreme cases one can expect to overestimate the age by ~10% or so, but for many grains the effect is much less.

Taking advantage of multiple single grain analyses, and considering that the Type II grains are statistically much less common than Type I fragments, we propose that a practical solution to the $L_0$ problem is to simply apply a constant and sufficiently long $L_0$ value to each fragment. This simplification is used in the following experiments. We found that a good value for $L_0$ was given by the maximum fragment length plus two times the maximum radius of a given set of fragments.

An important observation from this analysis of fragment age versus initial grain lengths in the context of inverting the observed ages to obtain a thermal history is that the helium diffusion profile within the core of the grain is insensitive to the estimated initial length (Fig. 4c). This follows because the diffusion profile within the core section of the grain (i.e., $>R_0$ from the ends of the cylinder), is set by the radial diffusion only. This is important because it demonstrates that when searching for viable thermal histories it is not possible to compensate for histories that are 'too hot' or 'too cold' by adjusting the estimated initial grain length, i.e., there is no trade-off between degree of heating and grain length.

It is possible to treat each initial grain length as an unknown parameter to be estimated along with the unknown thermal history, and this approach is illustrated by a simple experiment summarised in Fig. EA-1. In this

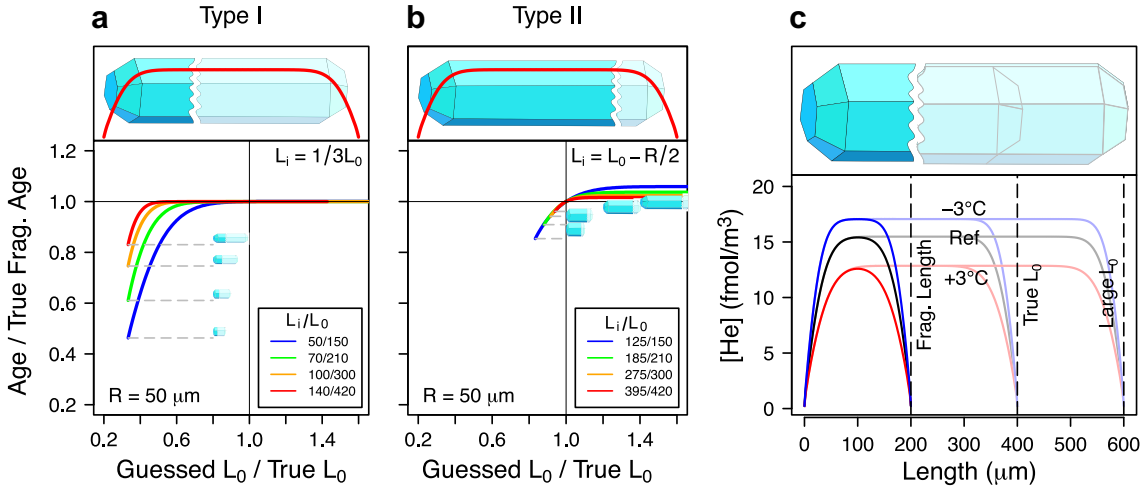


Fig. 4. Dealing with the $L_0$ problem. (a) Plots of relative apparent AHe ages for a range of fragment sizes for fragments of Type I versus relative assumed initial lengths, $L_0$. The thermal history used to generate ages was WOLF-5 because it produces well rounded diffusion profiles ideal for this analysis. For Type I fragments it is clear that choosing a suitably large $L_0$ yields a perfect prediction of the true fragment age. (b) Plots of relative apparent AHe ages for a range of fragment sizes for fragments of Type II versus relative assumed initial lengths, $L_0$. Choosing a large $L_0$ value for Type II fragments introduces an error by overpredicting the model AHe ages, but this error is typically less than c. 10%. (c) Plot of the axial diffusion profiles for three grains with increasing lengths derived for the WOLF-5 history and for the same history with a difference of +3 and −3 °C on the maximum temperature. Increasing the length of a grain of constant radius does not change the concentration within the core of the grain. This illustrates why there is no trade-off between choosing a thermal history that is too cold or too hot, and offsetting this mistake by fitting initial whole grain lengths that are too short or too long, respectively.

case we selected 3 Type I and 3 Type II fragments for the WOLF-5 history and ran an inversion test where we searched for the *t–T* history and the 6 initial grain lengths as 6 additional unknowns. The results illustrate that the optimisation does yield good estimates of the $L_0$ values, especially for Type II grains, which are more sensitive to this parameter. This approach is computationally expensive and so we suggest the simplification described above is a better approach for routine applications.

Handling 0T fragments will require the estimation of the initial grain length and the position of the fragment relative to the ends of the grain, thus introducing an additional unknown parameter for each fragment. Harnessing the additional information inherent in the added dispersion arising from including 0T fragments would be beneficial for constraining the thermal history inversions, but this aspect of the optimisation is beyond the scope of this paper. In the following inversion experiments we therefore restrict ourselves to using whole grains and 1T fragments.

### 4.3. Examples: Inversion of synthetic datasets

In the following we present a set of inversions using synthetic data sets generated for the five WOLF *t–T* histories which represent a good range of geologically plausible thermal histories. For each inversion, we report the range of acceptable paths in colour (darker blue is better) while the ensemble of models rejected appears in light grey. The best fit model (red lines) and average model (black lines) over all acceptable paths are also reported and compared to the thermal histories used to generate the synthetic data sets (thick, dashed yellow line). Full analysis of the data and model fits and Bayesian estimates of the 2D marginal probability-density functions of the *t–T* points and tables listing the expected *t–T* values with uncertainties are provided in the Electronic Annex. The expected model resulting from the Bayesian analysis is shown as the thin, dashed orange lines. In all cases the 'observed' data for these inversion experiments are the AHe fragment ages calculated using the forward model for the appropriate WOLF *t–T* history, the grain dimensions and the U and Th concentrations of each grain/fragment. The 'analytical error' on these synthetic ages was set at a nominal 5%, and for the experiments using synthetic data acceptable models defined as those where the predicted ages are within 5% of the age generated by the forward model. Detailed input fragment lists for all experiments, including relevant kinetic parameters, are tabulated in the Electronic Annex.

#### *4.3.1. Treating fragments and whole grains as spheres, Model#2 & Model#3*

To illustrate the consequence of inverting the AHe ages for a set of fragments without explicitly treating them as fragments coupled with using the spherical equivalent grain size transformation we performed a set of inversions using 25 fragments randomly generated from a single standard grain with $L_0 = 400$ μm and $R_0 = 75$ μm. Note that the dispersion in AHe fragment ages in this case is caused only by the effect of fragmentation because all fragments were cut from the same initial grain. The fragment ages were determined using the finite cylinder model as described above and the spherical equivalent radii were determined for the fragments using the actual fragment dimensions as in Eq. (20). In this case the inversion was performed using the ingrowth-diffusion model in its spherical geometry mode (see Appendix B). So here we are treating cylindrical

fragments as if they were whole spheres, which is currently routine practice. The results of these experiments are summarised in Fig. 5.

Only the inversion performed on the data set generated from the WOLF-1 thermal history yielded a result close to the true answer. This is not unexpected as the WOLF-1 history produces minimal fragment dispersion and grains of all sizes yield similar AHe ages because the cooling is linear and rapid. However, the fit to the data is poor (when comparing the input ages to those predicted by the expected model, see Fig. EA-2) and the results would likely be regarded as problematic. Surprisingly, the four other inversions yielded reasonable fits to the input ages but failed to return the correct thermal histories. In these cases, interpretation of the model *t–T* paths would be problematic. This model highlights a significant problem with using input AHe ages for crystals that are broken, but treating them as if they were whole grains. For completeness we also ran this experiment again, but using the whole grains rather than the fragments (Model#3). The results of this experiment are shown in Figs. EA-4, EA-5 and EA-6 and illustrate that the best fit model *t–T* histories derived using the inversion procedure fit the input *t–T* history quite well, and that the data fit is much better than that for fragment ages, confirming that the SEQR approximation and a 1D spherical solution works well when applied to whole crystals.

#### *4.3.2. Treating fragments as cylinders, Model#4*

In this experiment we used the same set of 25 1T fragments as those in the previous section, but in this case the inversion was performed using the new approach where the broken grains are treated explicitly as fragments of larger crystals using our finite cylinder model (Fig. 6). All five inversions resulted in good fits between observed and predicted ages, and most importantly produced reasonably good estimates of the true thermal histories (Figs. EA-7 and EA-8). We emphasise that this is a deliberately artificial but stringent test of the information recorded by fragment dispersion alone because all the fragments were effectively derived from the same standard grain, and so there is no other information about the style of the thermal history (e.g., absolute grain size) was available to constrain the inversion. This experiment shows that sufficient information on the thermal history to effectively resolve the ambiguity issue can be extracted from a set of broken crystals by explicitly treating them as fragments.

#### *4.3.3. Fragmentation and grain-size effect combined, Model#5*

In practice, when analysing grains from real samples, there will always be a range of true grain sizes available and it is common practice when applying the (U–Th)/He technique to perform analyses on a range of grain sizes. This is especially true if it is suspected that the sample may have experienced a complex thermal history. The aim is to exploit the grain-size effect as described first by Reiners and Farley (2001). It is now standard practice to look for correlations between single grain AHe ages and grain size (typically measured as the spherical equivalent radius), and/or eU (where eU is the effective uranium content given by [U] + 0.235[Th]). However, we have shown elsewhere (Brown et al., 2013, this volume) that simple correlations between AHe ages and grain size or eU can be disrupted because of the competing effects of both grain size and eU and thirdly because fragmentation further decouples these relationships. This observation is supported by many studies which document 'unexplained' dispersion where there are no obvious correlations between AHe ages and size or eU despite quite strong dispersion in the ages for a given sample (Fitzgerald et al., 2006; Kohn et al., 2009).

Given our analysis of the possible sources of dispersion (Brown et al., 2013, this volume) we suggest that in many cases strongly dispersed data can be robustly inverted to obtain useful thermal history information by focusing on modelling the dispersion arising from all possible causes explicitly. As a demonstration of this approach in this experiment we have generated 25 random 1T grain fragments from 25 randomly sized whole grains (Fig. 7). In this case it is clear that the amount of age dispersion is severe, especially for the histories that yield significant partial diffusional loss of helium, i.e., WOLF 3, 4 and 5. Despite this severe, and apparently random pattern of dispersion, the inversion procedure produces good fits to the data and yields fairly good estimates of the true thermal histories (Figs. EA-9 and EA-10).

### 4.4. How many grains are needed and what about noisy data? Model#6

Inversion of a set of AHe ages relies on the assumption that all the crystals have experienced a common thermal history, and that any dispersion in the data is caused solely because of effects which are a function of the thermal history. So two key questions arise. How many single grain AHe ages are needed to constrain the 'good' natural pattern of dispersion, and what about other sources of dispersion that simply add 'noise' rather than information? Typical analytical error is usually less than 5% of the age for a standard single grain analysis. Other factors such as spatial U, Th heterogeneities, fluid and/or mineral inclusions or $^{*}$He implantation can result in an extra source of dispersion, although typically this likely to be in the order of 10–15% (discussed in Brown et al., 2013, this volume). As a rule of thumb, one can assume that the more noisy the data, the more grains will be needed to insure that a sensible convergence is obtained, and the more 'good' dispersion the better.

To some extent the pattern of 'good' dispersion can be influenced by controlling grain selection protocols. So, in addition to standard screening of grains for inclusions and good shape/form it would assist if very short fragments as well as very long fragments were selected (to maximise the fragment effect), as well as selecting as wide a range of grain widths as possible (to maximise the grain size effect). Prior screening for the likely homogeneity of U and Th content would also help, either by performing apatite fission track analyses first (fission track densities revealed in grain mounts provide good estimates of U distribution and concentration) or by LA-ICPMS analysis (e.g., Farley et al., 2011).

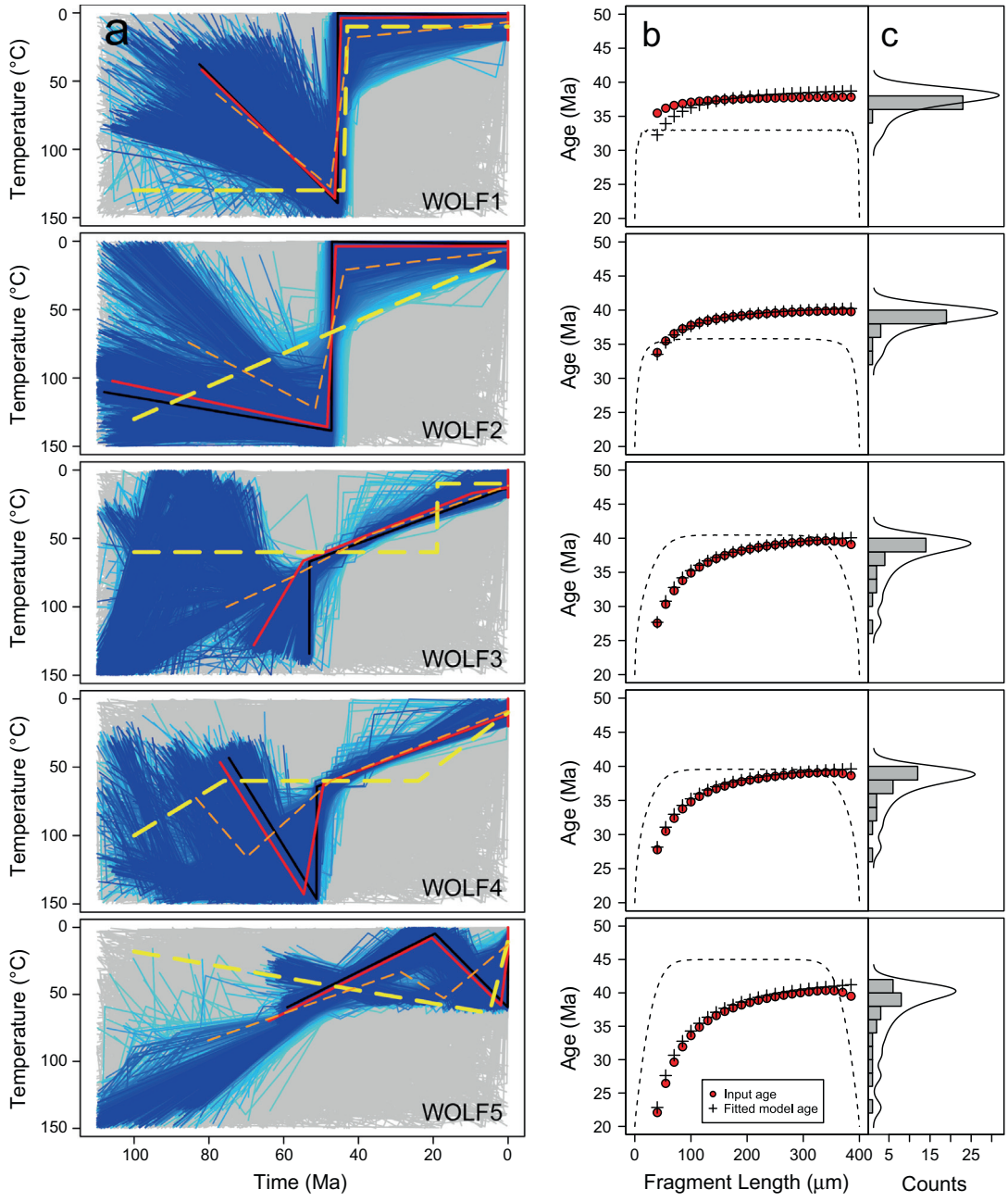


Fig. 5. Inverse modelling results of 25 synthetic 1T-cylindrical-fragment ages generated for the five WOLF thermal histories where the fragments are treated as whole spheres with equivalent surface/volume ratios as the fragments (see text for details). The 25 fragments were generated from a standard cylindrical grain with $L_0 = 400$ μm and $R_0 = 75$ μm and nominal U and Th concentrations of 20 ppm. (a) The thick dashed-yellow lines indicate the input thermal histories used to generate the fragment ages. The acceptable-fit field of solutions is shown by the blue shading (darker is better). The rejected field of solutions investigated by the NA algorithm is shown by the light-grey shading. The solid red lines represent the best-fit thermal histories while the solid black lines represent the average histories over the field of acceptable solutions. The dashed orange lines represent the expected model determined using Bayesian analysis of the complete model ensembles (Fig. EA-2). (b) The fragment ages predicted by the forward model (dashed yellow line) are indicated as red circles on the age dispersion fragment distribution (ADFD) plots. The predicted fragment ages for the best-models are indicated by black crosses. The dashed black lines indicate the normalised $^4$He axial diffusion profile for the whole grain. (c) The histograms represent the distribution of the fragment ages from the forward model while the solid black lines represent the predicted age distributions of the best-model thermal histories. No restrictions were placed on where the four $t$–$T$ pairs defining the thermal-history solutions were placed, other than within the bounds of the $t$–$T$ graphs. The only constraint imposed on the thermal history is the range of present-day temperatures indicated by the thick red lines. Detailed analysis of the model and data fits are provided in Figs. EA-2 and EA-3 and detailed input fragment lists including relevant kinetic parameters are provided for each model in the Electronic Annex. (For interpretation of the references to colour in this figure legend, the reader is referred to the web version of this article.)

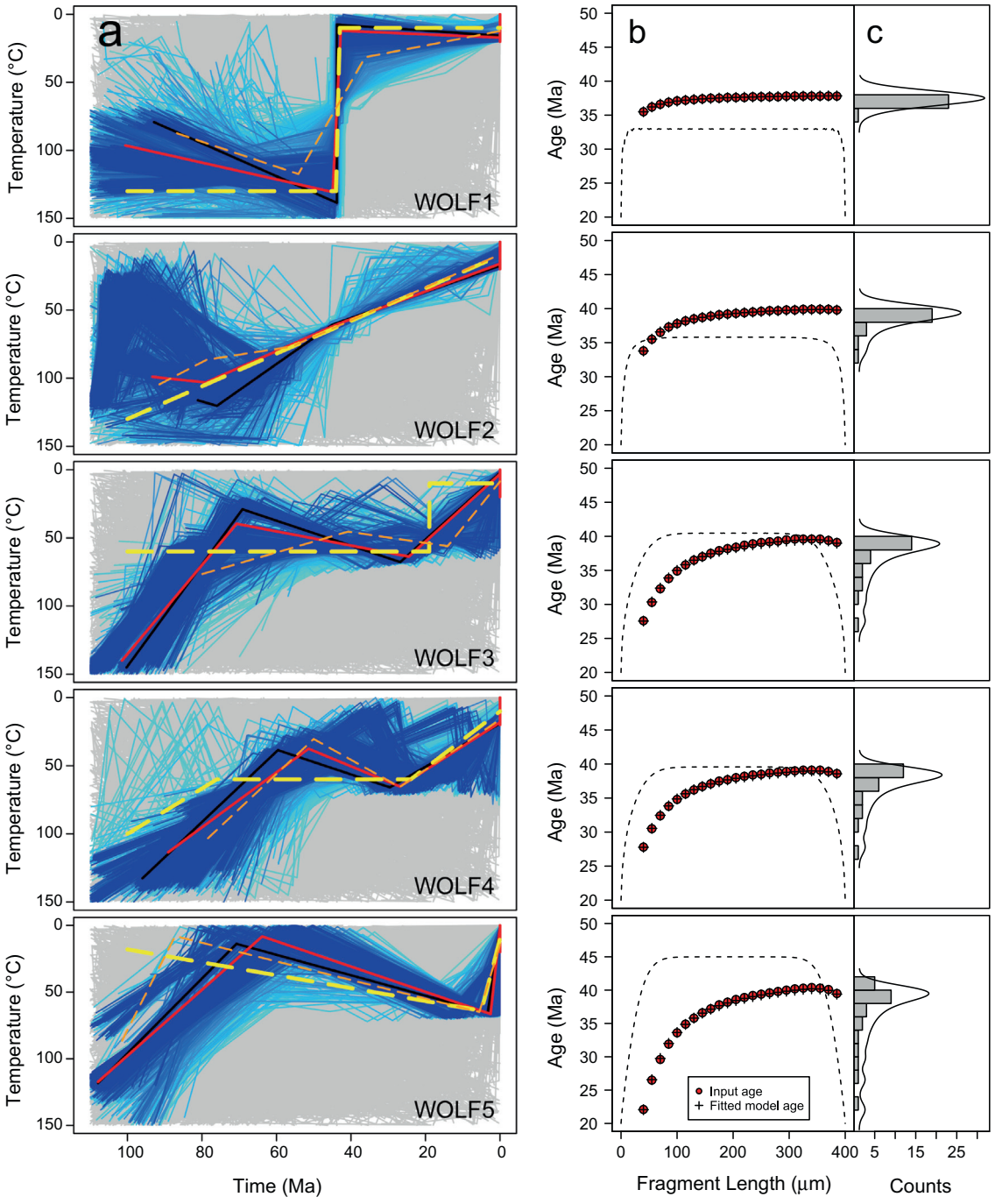


Fig. 6. Inverse modelling results of 24 synthetic 1T-cylindrical-fragment ages generated for the five WOLF thermal histories and treated explicitly as cylindrical fragments derived from a single standard grain (see text for details). The 25 cylindrical fragments were generated from a standard grain with $L_0 = 400$ μm and $R_0 = 75$ μm and nominal U and Th concentrations of 20 ppm. (a) The thick dashed yellow lines indicate the input thermal histories used to generate the fragment ages. The acceptable-fit field of solutions is shown by the blue shading (darker is better). The rejected field of solutions investigated by the NA algorithm is shown by the light-grey shading. The solid red lines represent the best-fit thermal histories while the solid black lines represent the average histories over the field of acceptable solutions. The dashed orange lines represent the expected model determined using Bayesian analysis of the NA ensemble (Fig. EA-7). (b) The fragment ages predicted by the forward model (dashed yellow line) are indicated as red circles on the age dispersion fragment distribution (ADFD) plots. The predicted fragment ages for the best-models are indicated by black crosses. The dashed black lines indicate the normalised $^4$He axial diffusion profile for the whole grain. (c) The histograms represent the distribution of the input fragment ages while the solid black lines represent the predicted age distributions of the best-model thermal histories. Detailed analysis of the model and data fits are provided in Figs. EA-7 and EA-8 and detailed input fragment lists including relevant kinetic parameters are provided for each model in the Electronic Annex. (For interpretation of the references to colour in this figure legend, the reader is referred to the web version of this article.)

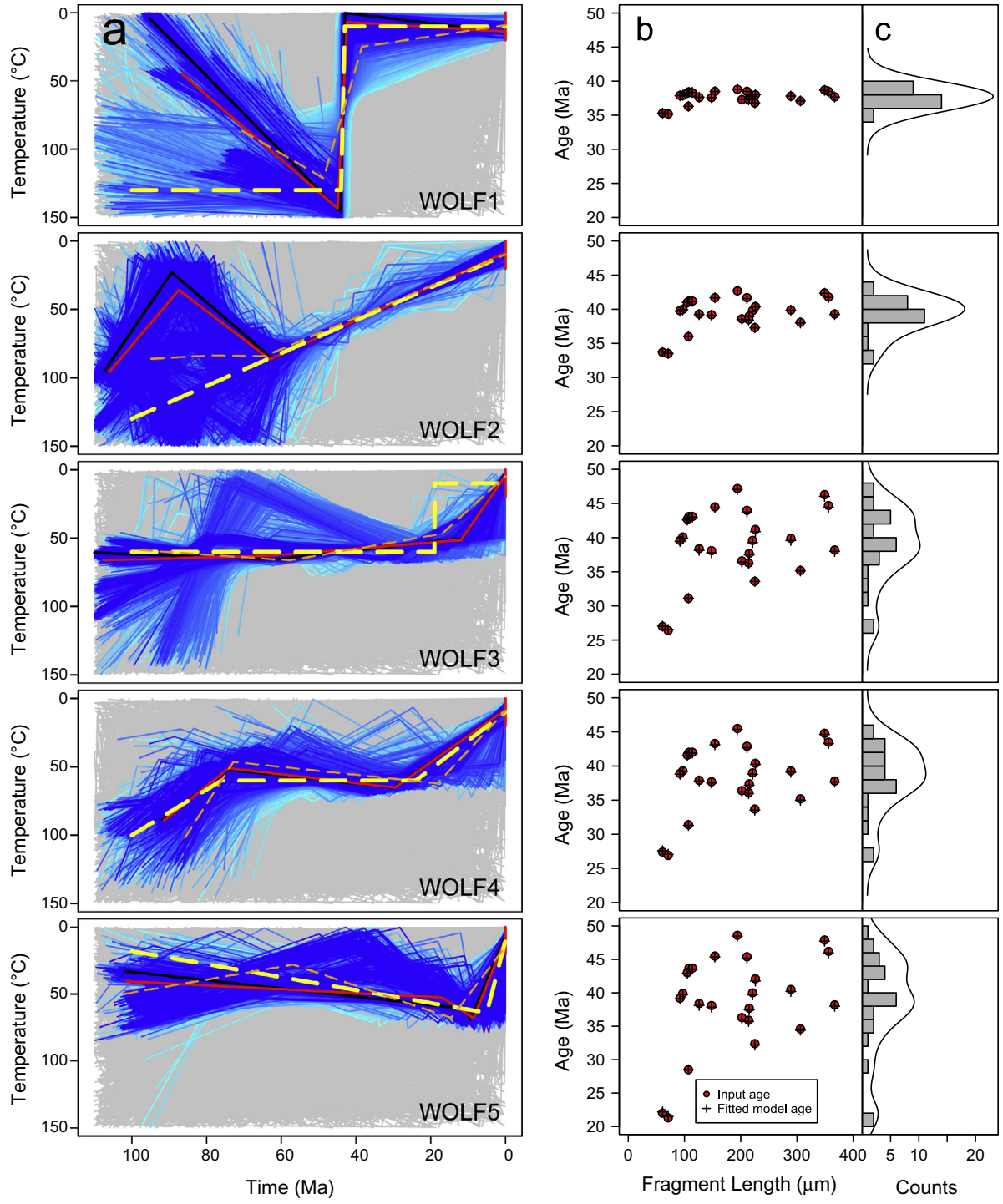


Fig. 7. Inverse modelling results of 25 synthetic 1T-cylindrical-fragment ages generated for the five WOLF thermal histories and treated as cylindrical fragments derived from a random set of longer grains (see text for details). The 25 cylindrical fragments were randomly generated using the following constraints: 200 µm $< L_0 <$ 600 µm; 50 µm $< R_0 <$ 100 µm; $2 < L_0/R_0 < 8$ all with nominal U and Th concentrations of 20 ppm. The thick dashed yellow lines indicate the input thermal histories used to generate the fragment ages. The acceptable-fit field of solutions is shown by the blue shading (dark is better). The rejected field of solutions investigated by the NA algorithm is shown by the light-grey shading. The solid red lines represent the best-fit thermal histories while the solid black lines represent the average histories over the field of acceptable solutions. The dashed orange lines represent the expected model determined using bayesian statistics (see Supplementary materials). Middle panels: The input fragment-ages are indicated as red circles on the age dispersion fragment distribution (ADFD) plots. The predicted fragment-ages for the best-models are indicated by black crosses. (c) The histograms represent the distribution of the input fragment ages while the solid black lines represent the predicted age distributions of the best-model thermal histories. Detailed analysis of the model and data fits are provided in Figs. EA-9 and EA-10 and detailed input fragment lists including relevant kinetic parameters are provided for each model in the Electronic Annex. (For interpretation of the references to colour in this figure legend, the reader is referred to the web version of this article.)

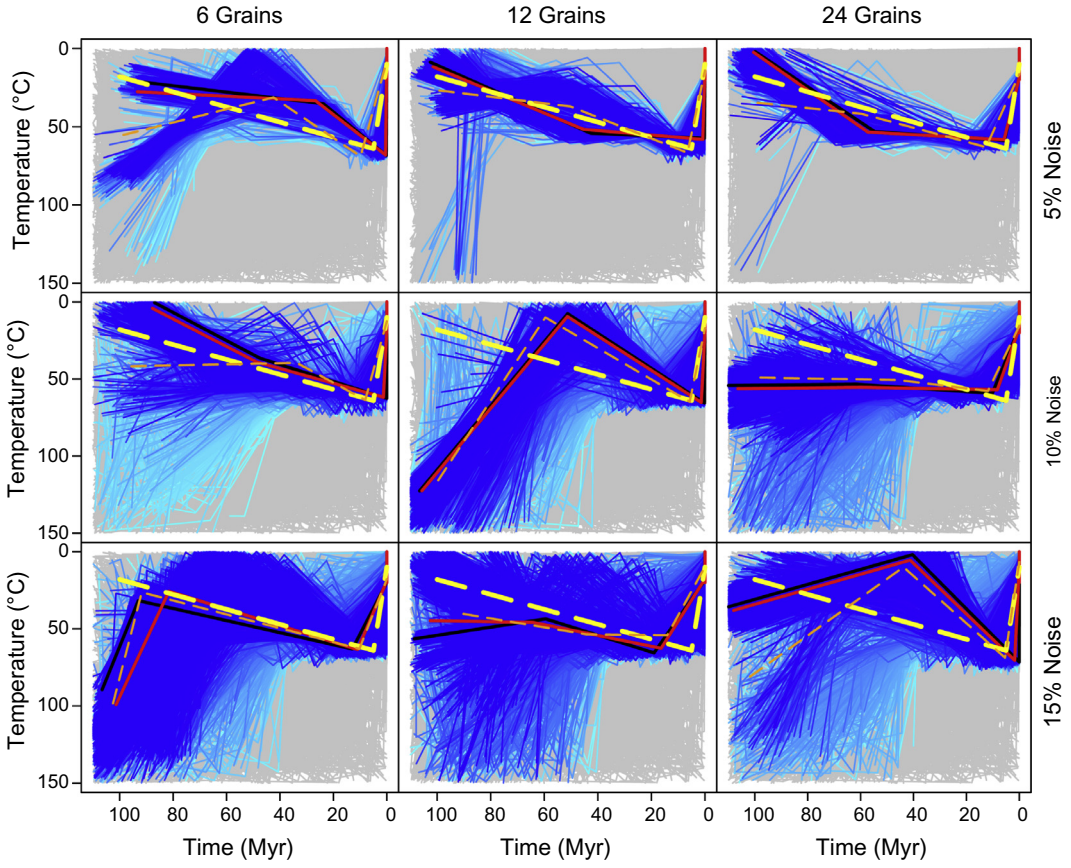


Fig. 8. Inverse modelling results using different numbers of fragments including different amounts of random noise. The 25 cylindrical fragments were generated from a single standard grain with $L_0 = 400$ μm and $R_0 = 75$ μm and U and Th concentrations of 20 ppm. The thick dashed-yellow lines show the input thermal history used to generate the fragment ages. The acceptable-fit field of solutions is shown by the blue shading (dark is better). The rejected field of solutions investigated by the NA algorithm is shown by the light-grey shading. The solid red lines represent the best-fit thermal histories while the solid black lines represent the average histories over the field of acceptable solutions. The dashed orange lines represent the expected model determined using the Bayesian analysis of the NA model ensemble (Sambridge, 1999b). Detailed input fragment lists including relevant kinetic parameters are provided for each model in the Electronic Annex. (For interpretation of the references to colour in this figure legend, the reader is referred to the web version of this article.)

To test the sensitivity of our approach to noisy data we ran an experiment using the WOLF-5 history as reference model. This model was chosen because it represents a realistic scenario where significant partial helium loss has occured leading to a large amount of useful dispersion. In this experiment we systematically tested the inversion using a range of grain numbers and amount of noise (added as a random % deviation to the individual synthetic AHe fragment ages). We ran inversions using 6, 12 and 24 grains with noise of 5%, 10% and 15% respectively (Fig. 8). This is a particularly stringent test because all the fragments were cut from a single standard grain with a nominal eU of 24 ppm, so that the only information about the thermal history style available to the inversion is the dispersion caused by fragmentation. In reality, absolute grain size as well as eU differences between grains could be used to further constrain the inversion process. Despite this limitation the results show that the method can easily deal with 5% noise typical of the uncertainty on well performed (U–Th)/He analyses, and unsurprisingly the greater the number of analysed crystals the better constrained the thermal history will be. For noise greater than 10%, the inversion clearly struggles to resolve the complexity of the thermal history, but interestingly the maximum temperature before final cooling seems to be relatively well constrained despite the noise. Adding a few 2T grains (whole grains) might in some cases help to counter the effects of noise and we thus suggest that good practice would involve picking mainly 1T fragments with some whole grains (if they exist) to perform the inversions. The number of grains required depends to some extent on the complexity of the history (which is unknown) and on the range of fragment sizes. Our results so far suggest that 15–20 grains would be a good number to start with.

#### 4.4.1. Including radiation damage and annealing, Model#7

The effect of radiation damage and annealing (Shuster et al., 2006) will potentially add a significant additional source of natural dispersion (e.g., Flowers et al., 2007, 2009; Ault et al., 2009; Flowers and Kelley, 2011). So including the effect of differential radiation damage should lead to even better constraints on the inversion performance because variations in eU between grains will produce large differences in AHe ages. To demonstrate this

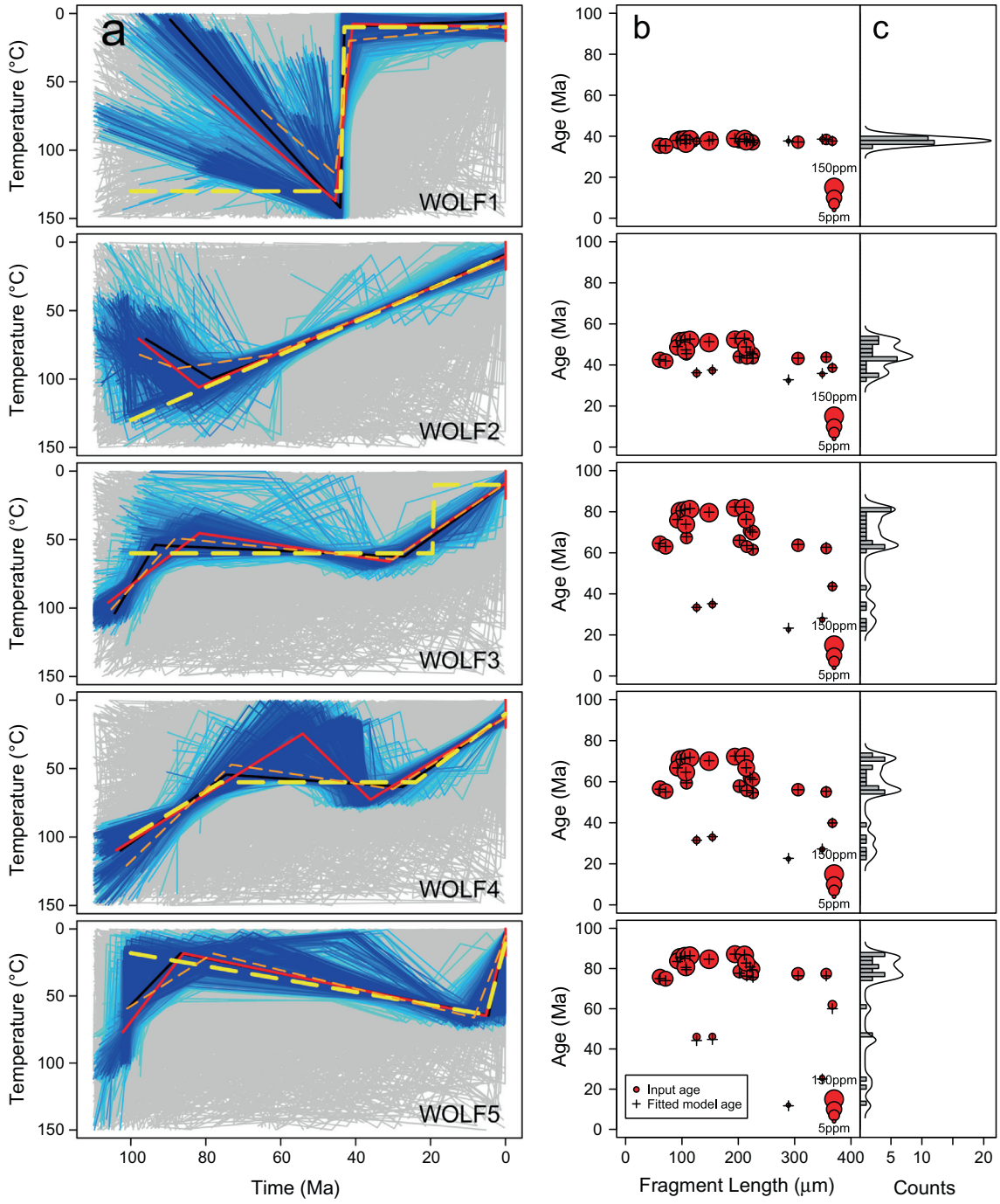


Fig. 9. Inverse modelling results of 25 synthetic 1T-cylindrical-fragment ages generated for the five WOLF thermal histories from a set of random grains with variable eU concentrations. The whole grain spherical equivalent radii range from 74 to 122 µm with eU from 8 to 150 ppm. (a) The thick dashed yellow lines indicate the input thermal histories used to generate the fragment ages. The acceptable-fit field of solutions is shown by the blue shading (darker is better). The rejected field of solutions investigated by the NA algorithm is shown by the light-grey shading. The solid red lines represent the best-fit thermal histories while the solid black lines represent the average histories over the field of acceptable solutions. The dashed orange lines represent the expected model determined using Bayesian analysis of the NA ensemble (Fig. EA-11). (b) The fragment ages predicted by the forward model (dashed yellow line) are indicated as red circles on the age dispersion fragment distribution (ADFD) plots. Note that the size of the circles indicates the eU content of the fragment (see legend). The predicted fragment ages for the best-models are indicated by black crosses. (c) The histograms represent the distribution of the input fragment ages while the solid black lines represent the predicted age distributions of the best-model thermal histories. Detailed analysis of the model and data fits are provided in Figs. EA-11 and EA-12 and detailed input fragment lists including relevant kinetic parameters are provided for each model in the Electronic Annex. (For interpretation of the references to colour in this figure legend, the reader is referred to the web version of this article.)

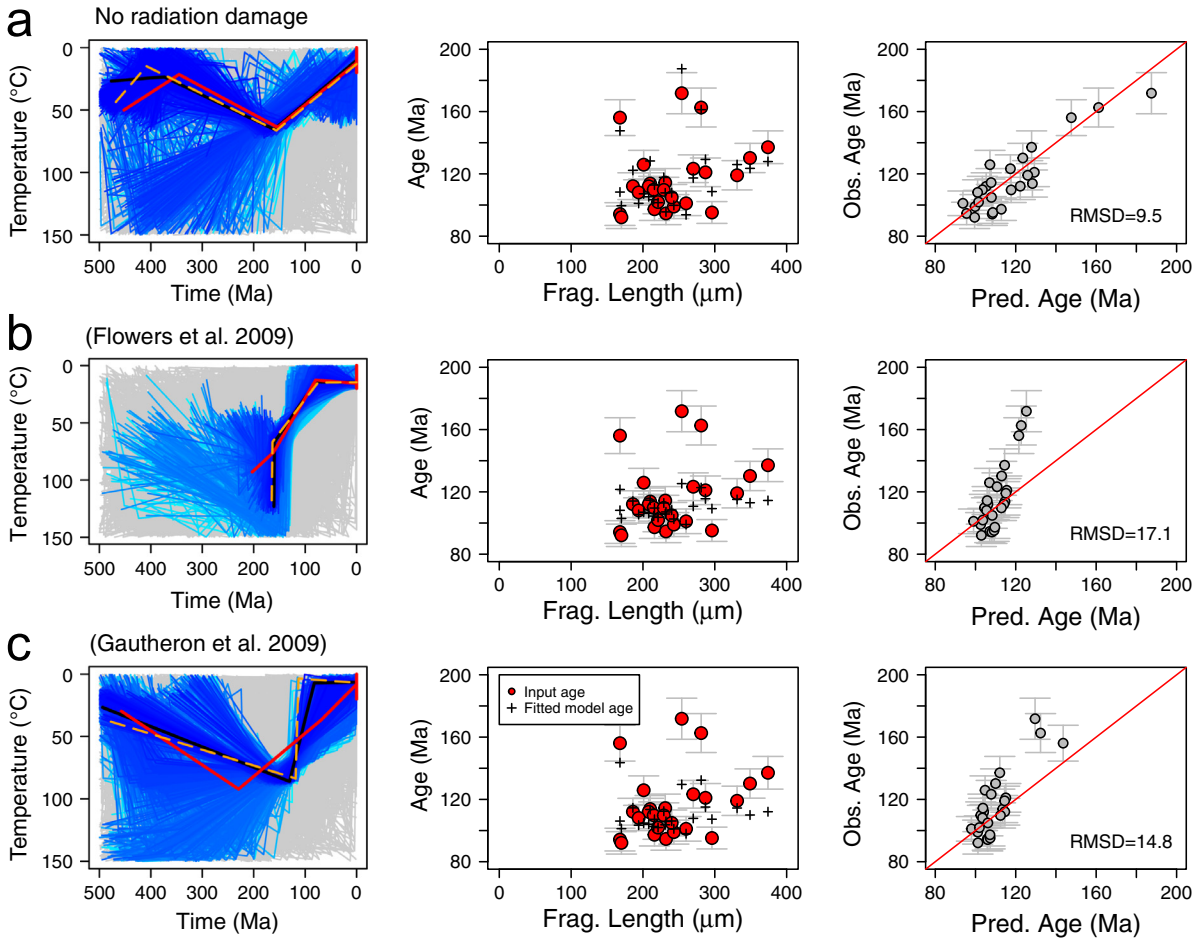


Fig. 10. Inverse modelling results for experiments using real data from sample BK1-650. (a) Results of inversion using the fragmentation model and standard diffusion kinetics of Farley (2000) and excluding radiation damage effects. The acceptable-fit field of $t$–$T$ solutions is shown by the blue shading (darker is better). The rejected field of solutions investigated by the NA algorithm is shown by the light-grey shading. The solid red lines represent the best-fit thermal histories while the solid black lines represent the average histories over the field of acceptable solutions. The dashed orange lines represent the expected model determined using Bayesian analysis of the NA ensemble (Figs. EA-13 and EA-14). The data fit is illustrated on an ADFD plot (central panels) with the observed ages shown as the red circles and the predicted ages by the black squares. The data fit is also assessed by plotting the observed ages versus the ages predicted by the best model (right panels). The 1:1 line on these plots is indicated by the solid black line. The std. errors for the observed ages are from Table EA-2. The goodness of fit is compared using the root mean squared difference (RMSD) between the observed and the predicated ages for each model. (b) Inversion experiment using fragmentation model incorporating the RDAAM model of Flowers et al. (2009). (c) Inversion experiment using the radiation damage accumulation and annealing model of Gautheron et al. (2009). (For interpretation of the references to colour in this figure legend, the reader is referred to the web version of this article.)

effect we ran an experiment using the RDAAM model of Flowers et al. (2009) for a set of 25 random fragments derived from a random set of whole grains with variable size ($R^*$, 74–122 μm) and U and Th concentrations (eU, 8–146 ppm) (see Table EA-1). The results of this experiment are illustrated in Figs. 9, EA-11 and EA-12. The data fit achieved in these experiments is indeed excellent, and is very similar to that achieved for Model#5 (fragments and grain size only). Including radiation damage as an additional natural source of dispersion does improve the inversion performance as indicated by the significant improvement in the constraints on the predicted $t$–$T$ models (see Figs. EA-11 and EA-12).

## 5. RESULTS FOR AN EXPERIMENT USING REAL DATA

To test and demonstrate the viability of our approach using real data we performed experiments (Model#8) using 25 new AHe single grain ages for a sample from the Bushveld Complex in South Africa (Table EA-2). The sample (BK1-650) is a ferro-gabbro collected at a depth of 650 m from the Bierkraal (BK-1) borehole which is located 100 km north-west of Johannesburg at an elevation of 1508 m (e.g., Kruger et al., 1987). Unpublished apatite fission-track analyses performed on a sample from BK-1 at a depth of 631 m yielded an AFT age of 351 ± 42 Ma with a

track length distribution showing a rather broad distribution and a short mean track length of $12.7 \pm 0.32$ μm. The apatite fission track data indicate that the sample has a complex thermal history and likely cooled to its present day down hole temperature of c. 34 °C at some time significantly younger than 351 Ma. Joint inversion of AFT data obtained for eight samples from different depths within the BK-1 borehole indicated a thermal history with protracted residence within the AFT partial annealing zone (c. 90–65 °C) between c. 400–100 Ma followed by accelerated cooling to surface temperatures (see Fig. 10 of Gallagher et al. (2005)).

The (U–Th)/He analyses were performed on 1T fragments ($168 < L_i < 374$ μm; $44 < R_i < 117$ μm) (Table EA-2) at the Scottish Universities Environmental Research Center (SUERC) using standard analytical procedures (e.g., Persano et al., 2002). The AHe ages show large dispersion with uncorrected ages ranging between $92 \pm 9.8$ Ma to $172 \pm 15.1$ Ma. All grains have similar eU concentrations with a mean of $12.5 \pm 4.5$ ppm suggesting they should have similar diffusion characteristics and the dispersion arising from radiation damage would be moderate or small.

We ran three separate inversion experiments using the real data. For these inversions we used the log-likelihood estimate as described by Gallagher et al. (2005) as the model misfit value to be minimised, because this explicitly accounts for the analytical uncertainties on the observed ages. This estimate essentially estimates the probability of obtaining the observed data from a given model in the ensemble with the analytical errors on observed ages explicitly used in the estimate of these probabilities. In the first experiment we used our fragmentation model and standard diffusion kinetics (Farley, 2000) excluding the radiation damage and annealing effect, in the second we combined our fragmentation model with the RDAAM model of Flowers et al. (2009) and in the third we incorporated the radiation damage model of Gautheron et al. (2009). The results of these experiments are summarised in Figs. 9, EA-13 and EA-14. In all cases the inversion converged well and yielded apparently well constrained thermal histories, although there are significant differences between the three models. The data fit for the fragmentation model excluding radiation damage effects is quite good, yielding a root mean squared deviation (RMSD) of 9.5 Ma (c. 10% of the mean grain age) with the data fit being reasonable but significantly poorer for the Flowers et al. (2009) and Gautheron et al. (2009) radiation damage models which yielded RMSD values of 17.1 Ma (c. 17%) and 14.8 Ma (c. 15%), respectively (Fig. 9). The thermal history obtained using our fragmentation model without radiation damage is consistent with the thermal history independently derived from the AFT data for this borehole (Gallagher et al., 2005). The thermal history obtained by incorporating the radiation damage model of Gautheron et al. (2009) is quite similar, but with more rapid cooling indicated during the mid Cretaceous. The thermal history obtained by the inversion incorporating the RDAAM model of Flowers et al. (2009) also implies rapid cooling in the mid Cretaceous, but from high temperatures of c. 100–110 °C which is close to the base of the AFT partial annealing zone. These differences in the thermal histories are directly related to the lower helium diffusivities (i.e., increased effective closure temperature) that are implied by the radiation damage models for the observed eU concentrations. Including radiation damage into the inversions causes the histories to cool from higher maximum palaeotemperatures. All models though seem to indicate a similar time of cooling at some time between 100 and 150 Ma (Fig. 10).

We believe that these inversion tests demonstrate the efficacy of our new approach for two reasons. Firstly they demonstrate that our inversion approach can yield stable estimates of the thermal history, as well as good fits to the observed data, for a real data set which shows quite extreme dispersion. Secondly, it demonstrates that the technique yields thermal history estimates that are consistent with independent estimates of the thermal history derived from apatite fission track analysis. This suggests that the good fit to the data is unlikely to be purely fortuitous and that the estimated thermal history is geologically meaningful.

These tests also raise some important questions concerning the parameterisation of the current radiation damage accumulation and annealing models (Flowers et al., 2009; Gautheron et al., 2009). Because these models produce such a large effect on the calculated diffusion rate of helium for histories such as these, where the sample spends an appreciable time within the helium partial retention zone, small differences in parameterisation can cause large differences in the predicted AHe ages. We suggest that the reason our model performs better when radiation damage is excluded, in this case at least, is because all the grains have quite low and very similar eU concentrations and so the radiation damage effect is likely quite small and similar for all grains. Any real errors in the parameterisation of the radiation damage models though will amplify differences in predicted ages based on their observed eU values making the convergence more difficult and yielding poorer data fits. This indicates that further and more detailed analysis of the radiation damage accumulation and annealing phenomenon is warranted, particularly with the aim of improving the constraints on parameterisation as well as investigating additional causes of variation in response, such as the compositional effect on the rates of damage annealing in apatite (e.g., Carlson et al., 1999; Barbarand et al., 2003; Gautheron et al., 2013).

## 6. CONCLUSIONS

Our new numerical approach explicitly treats broken apatite grains as fragments of initially larger prismatic crystals. This is achieved by solving for thermal diffusion and ingrowth of helium in a finite cylinder geometry to approximate the prismatic geometry of typical apatite crystals used for (U–Th)/He thermochronometry. We showed that it is practically possible to exploit the information about the distribution of $^4$He within the grains, recorded by the pattern of dispersion of single grain AHe ages arising from fragmentation, to constrain the time–temperature history of a sample. The corollary was also shown to be problematic, in that if fragments are treated as if they are whole grains and their size is characterised using the spherical equivalent radius transformation (which is currently common practice)

then thermal histories that yield good fits to the data may well be obtained, but the histories may be spurious.

The main unknowns in our approach, apart from the $T$–$t$ history of course, are the original lengths ($L_0$) of the crystals being analysed. We show that while in theory it is possible to fit both the unknown thermal history and the unknown $L_0$ values simultaneously (for 1T fragments at least), in practice this can be easily simplified by using a common, long $L_0$ for all fragments.

The advantage of our approach is that it explicitly exploits the true grain size information as well has handling the fragmentation effect, and it can easily accommodate radiation damage accumulation-annealing models that predict differences in diffusivity arising from differences in effective eU concentration. It also provides a cost effective, simple alternative, and complementary, approach to the $^4$He/$^3$He thermochronometry technique (Shuster and Farley, 2004, 2005) that effectively deals with the ambiguity problem of determining thermal histories from single grain AHe ages. It has the added advantage of capitalising on the fact that in most cases apatite crystals extracted for thermochronometry analysis are broken.

We also conclude that grain selection and picking should focus on maximising the natural dispersion of AHe ages obtained from a sample, not minimising it. We recommend that best practice should aim to pick and analyse more fragments than whole grains, and that the thermal history constraints be obtained by modelling the age dispersion by explicitly treating broken grains as fragments of larger grains as appropriate. In the unlikely event that fragments are rare and whole grains are abundant, then it may be beneficial to deliberately break whole grains to yield usable fragments, although this remains to be demonstrated experimentally. Perhaps, the best constraints on a region's thermal history could be obtained practically by applying our new approach but analysing many more grains (c. 15–20) from each sample than is typical at present, but from fewer samples. Coupling this strategy with judicious/surgical application of the $^4$He/$^3$He technique on key samples, where 2T whole grains were available, would be an ideal combination of techniques.

## ACKNOWLEDGEMENTS

We thank Kerry Gallagher for many stimulating discussions on the philosophy and application of optimisation techniques and thermochronometry modelling in general, and for his help with including the RDAAM code into HelFrag, Rich Ketcham and Sean Willett for their incisive comments and suggestions on previous presentations of this work which added significantly to the clarity of this paper, and Alexis Ault, Ryan McKeon and Pieter Vermeesch for their comprehensive and constructive reviews of the manuscript. Thanks also to Mark Mitchell and the ScotGrid staff for their assistance with MPI protocols and accessing the grid computing facilities at the University of Glasgow. This research was supported by NERC Grants NE/J013242/1 and NE/H008276/1 held at GU and NE/H008454/1 held at SUERC.

## APPENDIX A. DEFINITION OF THE α-EJECTION OPERATOR $\mathcal{L}_i$

One way to account for α-particle ejection is to alter the production of $^4$He from the source in appropriate way within an appropriate region near the surface of the grain. Eq. (6) allows for a variable source (heterogeneous distribution of the parent isotopes) by specifying an appropriate linear functional operator $\mathcal{L}_i$. This can be done by specifying a zone near the boundary of the crystal from which α-particles from each parent isotope are ejected. For example in a cylindrical crystal that occupies the (non-dimensional) region $0 \leqslant r \leqslant 1$ and $0 \leqslant z \leqslant l$ we could specify $\mathcal{L}_i$ for each parent isotope $i$ as

$$\mathcal{L}_i[p_i] = E_i(r,z)p_i(r,z) \tag{A.1}$$

where

$$E_i(r,z) = \frac{1}{4}\left(1 + f\left(\frac{2z}{l} - 1, \frac{s_i}{l}\right)\right)(1 + g(r,s_i)) \tag{A.2}$$

and functions $f$ and $g$ are

$$f(x,y) = 1 - \frac{e^{-(x+1)/y} + e^{-(1-x)/y}}{1 + e^{-2/y}} \tag{A.3}$$

$$g(x,y) = 1 - \frac{I_0(r/y)}{I_0(1/y)} \tag{A.4}$$

where $s_i = S_i/R_0$ with $S_i$ being the ejection zone width for isotope '$i$' and $R_0$ is the cylindrical radius. $I_0$ is the zeroth-order modified Bessel function of the first kind. Note that $f(\pm 1, s_i) = 0$ and $g(1, s_i) = 0$. The $E_i(r,z)$ function has the property that it is 1/4 near the corners, 1/2 near the edges and 1 in the interior, with the α-stopping distances $s_i$ for each parent isotope, and yields a smooth behaviour between these values.

Including the function $E_i(r,z)$ into the eigenmode equations (see Eq. (12) in the text) now requires performing the individual integrals $M_{nm}$ which are written as

$$M_{nm} = \frac{\int_{z=0}^{l}\int_{r=0}^{1} \widehat{E}_i(r,z)\sin\left(\frac{n\pi z}{l}\right)J_0(\alpha_m r)r\ dr\ dz}{\left(\int_{z=0}^{l}\sin\left(\frac{n\pi z}{l}\right)^2 dz\right)\left(\int_{r=0}^{1}J_0(\alpha_m r)^2 r\ dr\right)} \tag{A.5}$$

and which yield the following solutions

$$M_{nm} = \frac{2\left(2 + \alpha_m^2 s_i^2\right)\left(8l^2 + n^2\pi^2 s_i^2\right)}{n\pi\left(4l^2 + \pi^2 n^2 s_i^2\right)\left(1 + s_i^2\alpha_m^2\right)\alpha_m J_1(\alpha_m)} \quad \text{for } n \text{ odd}$$

$$M_{nm} = 0 \quad \text{for } n \text{ even} \tag{A.6}$$

These solutions for the $M_{nm}$ integrals replace the integrals in Eq. (12) to yield the final mode equations to be solved defined in Eq. (14).

## APPENDIX B. SPHERICAL SOLUTION

Suppose we model a spherically symmetric crystal as a sphere of radius $R_0$. The scalings to obtain the non-dimensional terms are as in the cylindrical case.

The mode equations are then

Table A1

| Parameter | Definition |
|---|---|
| $z$, $r$ | Cylindrical coordinates, $z$ axial, $r$ radial |
| $L_0$, $R_0$ | Axial and radial dimensions of the cylinder |
| $t$, $t_f$ | Time, total model time |
| $T$, $T_{\min}$, $T_{\max}$ | Temperature, min., max. |
| $E_a$ | Activation energy, J mol$^{-1}$ |
| $R$ | Molar gas constant, 8.3144621 kg m$^2$ s$^{-2}$ K$^{-1}$ mol$^{-1}$ |
| $R_g^*$ | Spherical equivalent radius of whole grain |
| $R_f^*$ | Spherical equivalent radius of fragment |
| $D$ | Diffusivity, m$^2$ s$^{-1}$ |
| $D_0$ | Diffusivity at infinite temperature |
| $D_\parallel$, $D_\perp$ | Diffusivity $\parallel$ and $\perp$ to $z$ |
| $i$ | Parent isotope species |
| $N$ | Number of parent isotopes species |
| $n_i$ | Number of helium nuclei produced by $\alpha_i$ decay of parent isotope $i$ |
| $\alpha_i$ | Decay rate of parent isotope $i$ |
| $\tau_e$ | Characteristic timescale (e.g., 1 Myr) |
| $\tau_d$ | Characteristic time for diffusion across radius $R_0$ at temperature $T_{\max}$. $\tau_d = \left(R_0^2/\hat{d}\right)$ |
| $C$ | Concentration of helium |
| $P_i$ | Concentration of parent isotope '$i$' at start, time $t = 0$ |
| $P_i^f$ | Concentration of parent isotope '$i$' at end, time $t = t_f$ |
| $C$ | Characteristic concentration (used to scale $C$ and $P_i$) |
| $S_i$ | $\alpha$-Particle stopping distance for isotope '$i$' |
| $\mathcal{L}_i$ | Linear operator accounting for alpha ejection of helium due to $\alpha_i$ decay of isotope $i$ |
| $l$, $r$ | Axial and radial dimension, scaled by $R_0$ |
| $t'$, $t'_f$ | Time, total model time, scaled by $\tau_e$ |
| $\theta$ | Temperature such that $T(t) = T_{\max} - \Delta T\theta$ with $\theta$ between 0 and 1 |
| $\lambda_i$ | Decay rate $\alpha_i$, scaled by $\tau_e$ |
| $c$ | Concentration of helium scaled by $\bar{C}$ |
| $p_i$ | Uniform concentration of parent isotope '$i$' at time $t' = 0$, scaled by $\bar{C}$ |
| $p_i^f$ | Uniform concentration of parent isotope '$i$' at time $t'_f$, scaled by $\bar{C}$ |
| $s_i$ | Stopping distance for isotope '$i$', scaled by $R_0$ |
| $\hat{d}$ | $\hat{d} = d\exp\left[-\frac{E_a}{RT_{\max}}\right]$ |
| $\gamma$ | $(E_a\Delta T)/RT_{\max}^2$, with ($\Delta\ T = T_{\max} - T_{\min}$) |
| $\delta$ | $(\Delta T)/T_{\max}$ |
| $\alpha_m$ | The $m$th zero of $J_0(r)$ |
| $E_i$ | Function used to modify the source term to account for $\alpha$-ejection |
| $\mathcal{C}^n$ | The non-dimensional total amount of helium contained in a section of the cylinder from $z_1$ to $z_2$ |
| $\mathcal{C}^d$ | The dimensional concentration of helium within the slice of the cylinder |
| $\mathcal{M}^d$ | Total dimensional amount of $^4$He (in moles) |
| $J_0$ | Bessel function |
| $I_0$ | Zeroth-order modified Bessel function of the first kind |
| $m$, $n$ | Number of eigenmodes in the $r$ and $z$ directions, respectively |

$$\frac{\partial c_n}{\partial t'} = -\beta n^2\pi^2 c_n \exp\left[-\frac{\gamma\theta}{1-\delta\theta}\right] + 2\sum_{i=1}^{N}\lambda_i n_i e^{-\lambda_i(t'_f - t')} \times \int_0^1 \mathcal{L}_i\left[p_i^f\right]\sin(n\pi r) r\, dr \tag{B.1}$$

The appropriate functional modifying the source to account for $\alpha$-ejection from the rims of the grains is

$$\mathcal{L}_i[p_i] = E_i(r)p_i \tag{B.2}$$

where

$$E_i(r) = 1 - \frac{1}{r}\frac{e^{-(1-r)/s_i} - e^{-(1+r)/s_i}}{1 - e^{-1/s_i}} \tag{B.3}$$

with $s_i = S_i/R_0$ and $S_i$ is the ejection zone width for isotope '$i$'. So, including the appropriate integrals of $E_i(r)$ which are given by

$$\int_0^1 r\sin(n\pi r)E_i(r)\, dr = \frac{(-1)^{n+1}}{n\pi(1 + n^2\pi^2 s_i^2)} \tag{B.4}$$

into the mode equations defined in (B.1), yields the final mode equations to be solved, with this model for the source and a uniform concentration of each parent isotope, as

$$\frac{\partial c_n}{\partial t'} = -\beta n^2\pi^2 c_n \exp\left[-\frac{\gamma\theta}{1-\delta\theta}\right] + 2\sum_{i=1}^{N}\lambda_i n_i e^{\lambda_i\left(t'_f - t'\right)} \times \frac{(-1)^{n+1}}{n\pi(1 + n^2\pi^2 s_i^2)} p_i^f \tag{B.5}$$

The non-dimensional concentration of $^4$He at $t'$ can now be obtained by summing over all $n$ modes, as given by

$$c(r,t') = \sum_{n=1}^{\infty} c_n(t') \frac{\sin(n\pi r)}{r}. \quad \text{(B.6)}$$

## APPENDIX C. SUPPLEMENTARY DATA

Supplementary data associated with this article can be found, in the online version, at http://dx.doi.org/10.1016/j.gca.2013.05.042.

## REFERENCES


Ault A. K. and Flowers R. M. (2012) Is apatite U–Th zonation information necessary for accurate interpretation of apatite (U–Th)/He thermochronometry data? *Geochim. Cosmochim. Acta* **79**, 60–78.

Ault A. K., Flowers R. M. and Bowring S. A. (2009) Phanerozoic burial and unroofing history of the western Slave craton and Wopmay orogen from apatite (U–Th)/He thermochronometry. *Earth Planet. Sci. Lett.* **284**(1), 1–11.

Barbarand J., Carter A., Wood I. and Hurford T. (2003) Compositional and structural control of fission-track annealing in apatite. *Chem. Geol.* **198**(1), 107–137.

Beucher R., van der Beek P., Braun J. and Batt G. E. (2012) Exhumation and relief development in the Pelvoux and Dora-Maira massifs (western Alps) assessed by spectral analysis and inversion of thermochronological age transects. *J. Geophys. Res.* **117**(F3).

Brown R.W., Beucher R., Roper S., Persano C., Stuart F. and Fitzgerald P., Natural age dispersion arising from the analysis of broken crystals: Part I. Theoretical basis and implications for the apatite (U–Th)/He thermochronometer. *Geochem. Cosmochim. Acta*, doi:10.1016/j.gca.2013.05.041.

Carlson W. D., Donelick R. A. and Ketcham R. A. (1999) Variability of apatite fission-track annealing kinetics: I. Experimental results. *Am. Mineral.* **84**, 1213–1223.

Cherniak D., Watson E. and Thomas J. (2009) Diffusion of helium in zircon and apatite. *Chem. Geol.* **268**(1–2), 155–166.

Ehlers T. A. and Farley K. A. (2003) Apatite (U–Th)/He thermochronometry: methods and applications to problems in tectonic and surface processes. *Earth Planet. Sci. Lett.* **206**(1–2), 1–14.

Farley K., Shuster D. and Ketcham R. (2011) U and Th zonation in apatite observed by laser ablation ICPMS, and implications for the (U–Th)/He system. *Geochim. Cosmochim. Acta* **75**(16), 4515–4530.

Farley K. A. (2000) Helium diffusion from apatite: general behavior as illustrated by Durango fluorapatite. *J. Geophys. Res.* **105**(B2), 2903.

Farley K. A. (2002) (U–Th)/He dating: techniques, calibrations, and applications. *Rev. Mineral. Geochem.* **47**(1), 819–844.

Farley K. A., Shuster D. L., Watson E. B., Wanser K. H. and Balco G. (2010) Numerical investigations of apatite $^4$He/$^3$He thermochronometry. *Geochem. Geophys. Geosyst.* **11**(10).

Farley K. A., Wolf R. A. and Silver L. T. (1996) The effects of long alpha-stopping distances on (U–Th)/He ages. *Geochim. Cosmochim. Acta* **60**(21), 4223–4229.

Fitzgerald P., Baldwin S., Webb L. and O'Sullivan P. (2006) Interpretation of (U–Th)/He single grain ages from slowly cooled crustal terranes: a case study from the Transantarctic Mountains of southern Victoria Land. *Chem. Geol.* **225**(1–2), 91–120.

Flowers R., Shuster D., Wernicke B. and Farley K. (2007) Radiation damage control on apatite (U–Th)/He dates from the Grand Canyon region, Colorado Plateau. *Geology* **35**(5), 447–450.

Flowers R., Wernicke B. and Farley K. (2008) Unroofing, incision, and uplift history of the southwestern Colorado Plateau from apatite (U–Th)/He thermochronometry. *Geol. Soc. Am. Bull.* **120**(5–6), 571–587.

Flowers R. M. and Kelley S. A. (2011) Interpreting data dispersion and "inverted" dates in apatite (U–Th)/He and fission-track datasets: an example from the US midcontinent. *Geochim. Cosmochim. Acta* **75**(18), 5169–5186.

Flowers R. M., Ketcham R. A., Shuster D. L. and Farley K. A. (2009) Apatite (U–Th)/He thermochronometry using a radiation damage accumulation and annealing model. *Geochim. Cosmochim. Acta* **73**(8), 2347–2365.

Gallagher K. (2012) Transdimensional inverse thermal history modeling for quantitative thermochronology. *J. Geophys. Res.* **117**(B2), 1–16.

Gallagher K., Stephenson J., Brown R., Holmes C. and Fitzgerald P. (2005) Low temperature thermochronology and modeling strategies for multiple samples 1: vertical profiles. *Earth Planet. Sci. Lett.* **237**(1), 193–208.

Gautheron C. and Tassan-Got L. (2010) A monte carlo approach to diffusion applied to noble gas/helium thermochronology. *Chem. Geol.* **273**(3), 212–224.

Gautheron C., Tassan-Got L., Barbarand J. and Pagel M. (2009) Effect of alpha-damage annealing on apatite (U–Th)/He thermochronology. *Chem. Geol.* **266**(3–4), 157–170.

Gautheron C., Tassan-Got L., Ketcham R. A. and Dobson K. J. (2012) Accounting for long alpha-particle stopping distances in (U–Th–Sm)/He geochronology: 3D modeling of diffusion, zoning, implantation, and abrasion. *Geochim. Cosmochim. Acta* **96**, 44–56.

Gautheron C., Barbarand J., Ketcham R. A., Tassan-Got L., van der Beek P., Pagel M., Pinna-Jamme R., Coffignal F. and Fialin M. (2013) Chemical influence on α-recoil damage annealing in apatite: Implications for (U-Th)/He dating. *Chem. Geol.* **351**, 257–267.

Glotzbach C., van der Beek P. and Spiegel C. (2011) Episodic exhumation and relief growth in the Mont Blanc massif, Western Alps from numerical modelling of thermochronology data. *Earth Planet. Sci. Lett.* **304**(3–4), 417–430.

Herman F., Copeland P., Avouac J.-P., Bollinger L., Mahéo G., Le Fort P., Rai S., Foster D., Pêcher A., Stüwe K. and Henry P. (2010) Exhumation, crustal deformation, and thermal structure of the Nepal Himalaya derived from the inversion of thermochronological and thermobarometric data and modeling of the topography. *J. Geophys. Res.* **116**(B6).

Hindmarsh A. (1983) *ODEPACK: A Systematized Collection of ODE Solvers*. North Holland, Amsterdam.

House M. A., Farley K. A. and Kohn B. P. (1999) An empirical test of helium diffusion in apatite: borehole data from the Otway basin, Australia. *Earth Planet. Sci. Lett.* **170**(4), 463–474.

Ketcham R. A. (2005) Forward and inverse modeling of low-temperature thermochronometry data. *Rev. Mineral. Geochem.* **58**(1), 275–314.

Ketcham R. A., Gautheron C. and Tassan-Got L. (2011) Accounting for long alpha-particle stopping distances in (U–Th–Sm)/He geochronology: refinement of the baseline case. *Geochim. Cosmochim. Acta* **75**(24), 7779–7791.

Kohn B. P., Lorencak M., Gleadow A. J. W., Kohlmann F., Raza A., Osadetz K. G. and Sorjonen-Ward P. (2009) A reappraisal of low-temperature thermochronology of the eastern Fennoscandia Shield and radiation-enhanced apatite fission-track annealing. *Geol. Soc. Lond. Spec. Publ.* **324**(1), 193–216.

Kruger F., Cawthorn R. and Walsh K. (1987) Strontium isotopic evidence against magma addition in the upper zone of the bushveld complex. *Earth Planet. Sci. Lett.* **84**(1), 51–58.

Lovera O. M., Grove M. and Harrison T. M. (2002) Systematic analysis of K-feldspar $^{40}Ar/^{39}Ar$ step heating results: II. Relevance of laboratory argon diffusion properties to nature. *Geochim. Cosmochim. Acta* **66**(7), 1237–1255.

Meesters A. and Dunai T. (2002a) Solving the production–diffusion equation for finite diffusion domains of various shapes: Part II. Application to cases with α-ejection and nonhomogeneous distribution of the source. *Chem. Geol.* **186**(3–4), 333–344.

Meesters A. and Dunai T. (2002b) Solving the production–diffusion equation for finite diffusion domains of various shapes: Part I. Implications for low-temperature (U–Th)/He thermochronology. *Chem. Geol.* **186**(3–4), 333–344.

Persano C., Stuart F. M., Bishop P. and Barfod D. N. (2002) Apatite (U–Th)/He age constraints on the development of the Great Escarpment on the southeastern Australian passive margin. *Earth Planet. Sci. Lett.* **200**(1–2), 79–90.

Reiners P. W. and Brandon M. T. (2006) Using thermochronology to understand orogenic erosion. *Annu. Rev. Earth Planet. Sci.* **34**(1), 419–466.

Reiners P. W., Ehlers T. A. and Zeitler P. K. (2005) Past, present, and future of thermochronology. *Rev. Mineral. Geochem.* **58**, 1–18.

Reiners P. W. and Farley K. A. (2001) Influence of crystal size on apatite (U–Th)/He thermochronology: an example from the Bighorn Mountains, Wyoming. *Earth Planet. Sci. Lett.* **188**(3–4), 413–420.

Sambridge M. (1999a) Geophysical inversion with a neighbourhood algorithm: I. Searching a parameter space. *Geophys. J. Int.* **138**(2), 479–494.

Sambridge M. (1999b) Geophysical inversion with a neighbourhood algorithm: II. Appraising the ensemble. *Geophys. J. Int.* **138**(3), 727–746.

Shuster D. L. and Farley K. A. (2004) $^{4}He/^{3}He$ thermochronometry. *Earth Planet. Sci. Lett.* **217**(1), 1–17.

Shuster D. L. and Farley K. A. (2005) $^{4}He/^{3}He$ thermochronometry: theory, practice, and potential complications. *Rev. Mineral. Geochem.* **58**(1), 181–203.

Shuster D. L., Flowers R. M. and Farley K. A. (2006) The influence of natural radiation damage on helium diffusion kinetics in apatite. *Earth Planet. Sci. Lett.* **249**(3–4), 148–161.

Spiegel C., Kohn B., Belton D., Berner Z. and Gleadow A. (2009) Apatite (U–Th–Sm)/He thermochronology of rapidly cooled samples: the effect of He implantation. *Earth Planet. Sci. Lett.* **285**(1–2), 105–114.

Valla P. G., Herman F., van der Beek P. A. and Braun J. (2010) Inversion of thermochronological age-elevation profiles to extract independent estimates of denudation and relief history: I. Theory and conceptual model. *Earth Planet. Sci. Lett.* **295**(3–4), 511–522.

Valla P. G., van der Beek P. A., Shuster D. L., Braun J., Herman F., Tassan-Got L. and Gautheron C. (2012) Late Neogene exhumation and relief development of the Aar and Aiguilles Rouges massifs (Swiss Alps) from low-temperature thermochronology modeling and $^{4}He/^{3}He$ thermochronometry. *J. Geophys. Res.* **117**(F1).

Vermeesch P., Seward D., Latkoczy C., Wipf M., Günther D. and Baur H. (2007) α-Emitting mineral inclusions in apatite, their effect on (U–Th)/He ages, and how to reduce it. *Geochim. Cosmochim. Acta* **71**(7), 1737–1746.

Watson E. B., Wanser K. H. and Farley K. A. (2010) Anisotropic diffusion in a finite cylinder, with geochemical applications. *Geochim. Cosmochim. Acta* **74**(2), 614–633.

Wolf R., Farley K. and Kass D. (1998) Modeling of the temperature sensitivity of the apatite (U–Th)/He thermochronometer. *Chem. Geol.* **148**(1–2), 105–114.

*Associate editor:* David L. Shuster